สำนักงานวิทยทรัพยากร
จุฬาลงกรณ์มหาวิทยาลัย

CHAPTER IV
RESULTS AND DISCUSSION

4.1 Preliminary Study

In the present work, electrospraying of 1% (w/v) chitosan solution in 1% (v/v) lactic acid were performed to obtain a well form nanoparticles with uniform particle size and narrow size distribution. This technique is simple, fast and a unique one-step method. The information of electrospraying parameters more knownledge about the influences of fabrication parameters on the morphology and size of the particles and then using the obtained parameters to optimize the conditions for fabricating nanoparticles appropriate for drug delivery applications.

In the preliminary study, effects of various processes and parameters of electrospray on the size and morphology of the particles were studied and the results of the following were obtained:

i. effect of needle gauge
ii. effect of applied voltage
iii. effect of flow rate
iv. effect of working distance

Experiments conducted on each variable (while keeping other variables constant) take to the optimized value of that specific variable. This optimized value was then used for all further studies.

4.1.1 Effect of needle gauge

The diameter of a needle is inversely proportional to its gauge number and hence smaller needles have a higher gauge number. Needles of various gauges were used and their influence on the size and morphology of chitosan micro/nanosparticles was studied. The number of needle gauges used were 20, 24 and 26 gauge (g) (with internal diameter (I.D.) of 0.902, 0.559, and 0.457 mm, respectively). The voltage, flow rate, working distance and stirring rate were kept at 10 kV, 10 mL/h, 12 cm and

400 rpm, respectively. At needle gauge of 20 g, chitosan solution was intermittent sputtered and very small extent of irregular shape microparticles were approximately size over 20 μm (figure 4.1 a). As the needle gauge were increased to 24 and 26 g (internal I.D. decreased), the chitosan solution did not sputtered and only forming microparticles with quit spherical shape were formed. The dry particle size as measured by SEM decreased to about 12 and 10 μm, respectively (Figure 4.1 b-c).

In case of smaller number of needle gauge, the effective flow rate of polymer solution increases and the drops are formed very quickly. The polymer solution flow out from the needle tip freely and sputters without formation of particles. In case of higher needle gauge, the droplets are formed at a rate, which is optimum to allow for the spraying of the polymer solution with the formation of stable jet, which results in the formation of microparticles. The runs with 24 and 26 g substantiated this phenomenon. As diameter of the base of the Taylor cone closely reflects the internal diameter of the needle tip, thus the jet ejected out of 26g was finer than that of 24g. As particles using needle gauge 26 g had the smallest particle size. Therefore, needle gauge of 26 g was used for further experiments.

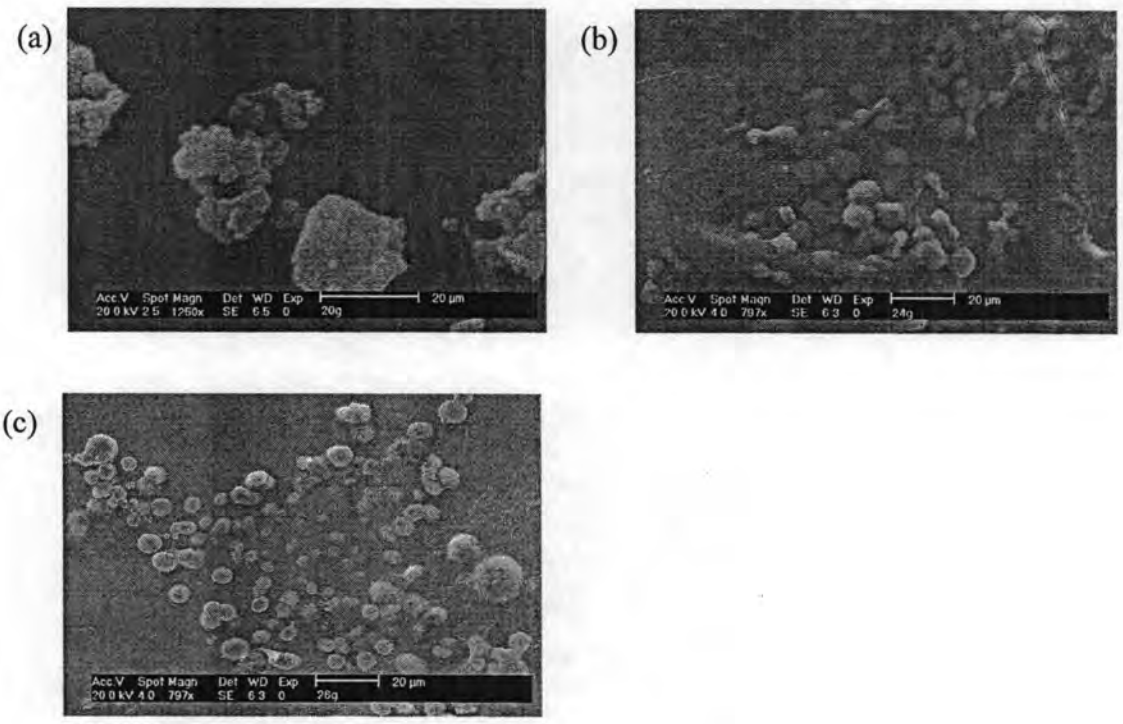

Figure 4.1 Effect of needle gauge on size measured by SEM (a) 20g (b) 24 g (c) 26g

Table 4.1 Effect of needle gauge on particle size of chitosan

Needle gauge (g)	Shape	Size
20	Irregular aggregated particles	〉20 μm
24	Irregular microparticles	~ 10 to 20 μm
26	Spherical microparticles	〈 10 μm

4.1.2 Effect of applied voltage

The effect of the applied voltage on particles formation is the next parameter to be studied by varying an applied voltage of 10, 13 and 15 kV. Higher and lower voltage in this range led to the irregular particle deposition with irregular shapes. When electric field is low, chitosan solution could flow freely and sputter unstably, so large beads with irregular shape are formed. At high voltage, the size of particles does not smaller than 15 kV.

While the needle gauge, the flow rate of the chitosan solution, the working distance and stirring rate were kept constant at 26 g, 10 mL/h, 12 cm and 400 rpm, respectively. The applied voltage affects the breakdown of the jet, so increasing voltages increases the jet current and leads to smaller particle sizes. From the SEM analysis of dry particles, as the voltage was increased from 10, 13 and 15 kV, the particles remained spherical but decreased in size by range of approximately from 10 to 8 μm, respectively (figure 4.3 a-c). However, the size of the particle at 15 kV is not clearly differ with the 13 kV.

These observed changes in the particle sizes can be attributed to the Rayleigh limit, that is the magnitude of charge on a drop that overcomes the surface tension force, leads to a fission of the droplet [30]. The applied voltage to the polymer solution causes the formation and accumulation of charge at the tip of the needle. At a lower applied voltage, there is only a low charge on each drop, so large spheres with

an irregular shape are formed. By increasing the applied voltage, the number of charge carriers in a jet segment is also increased. This results in an increase in both the electrostatic and the Coulombic forces. The increased Coulombic force provides more stretching force on the jet segment and should also result in more repulsion between adjacent droplets, resulting in individual particles and a smaller spherical size (Figure 4.2). Thus, an applied voltage of 13 kV was selected for further experiments.

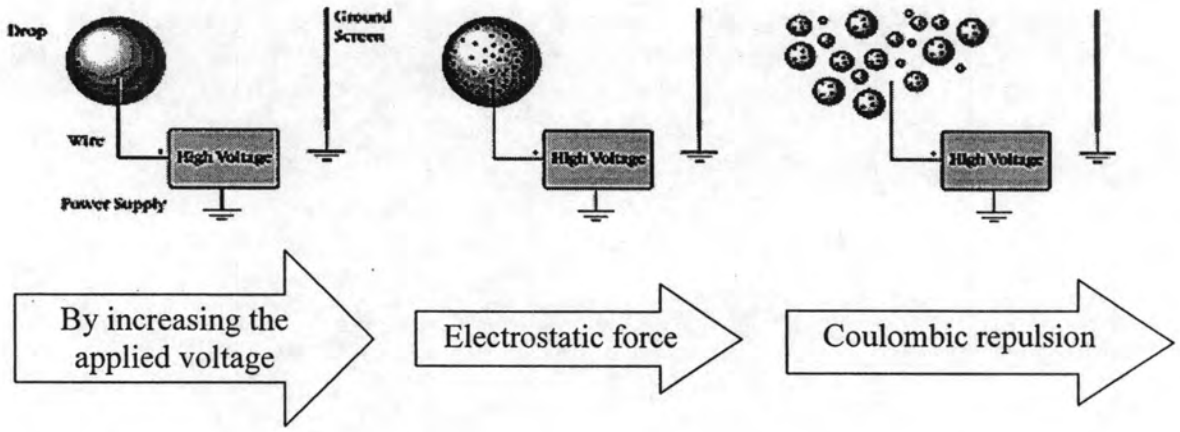

Figure 4.2 A diagram of the steps of electrospraying technique

(a)

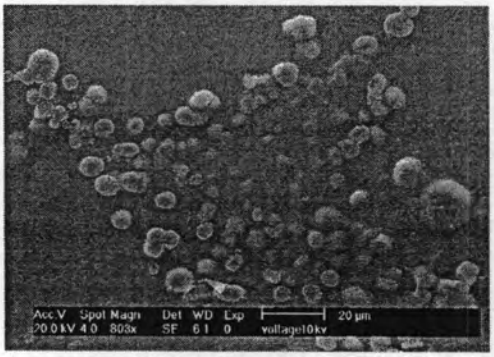

(b)

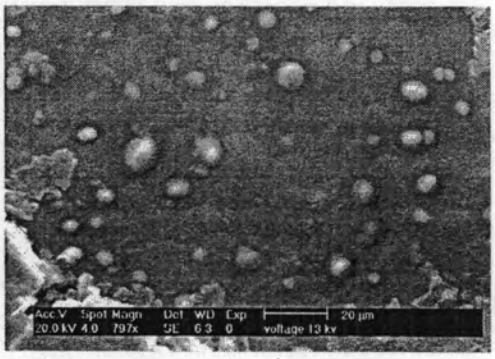

(c)

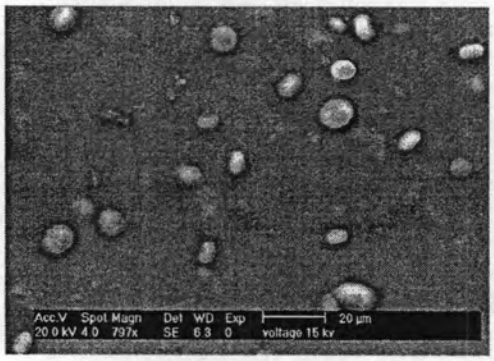

Figure 4.3 Effect of applied voltage on size measured by SEM (a) 10 kV (b) 13 kV (c) 15 kV

Table 4.2 Effect of applied voltage on particle size of chitosan

Applied voltage (kV)	Shape	Size
10	Spherical microparticles	~10 µm
13	Spherical microparticles	~8 µm
15	Spherical and ovary microparticles	~8 µm

4.1.3 Effect of the flow rate

In the next set of experiments, the effect of flow rate on particles formation was studied by using the experiments for different flow rate values of 0.5, 5, 10 mL/h, while the needle gauge, applied voltage, working distance and stirring rate were kept constant at 26 g, 13 kV 12 cm and 400 rpm, respectively. As the flow rate was increased from 0.5 to 10 mL/h, the particles increased in size approximately 1.5 to 10 μm, respectively for the dry particles (figure 4.4 a-c).

This increase in particle size with increasing chitosan flow rate can be simply explained by the fact that the solution flowing out of the needle causes an elongation of the meniscus to form a jet. Therefore, the optimum flow rate is when spraying of the polymer solution leads to the formation of a stable jet, and so to form smaller sized particles. Whereas, at a higher flow rate, the effective flow rate of the polymer solution increases and the drops are formed very quickly, leading to the formation of larger particle sizes. Thus, the flow rate of 0.5 mL/h was selected for further experiments.

(a)

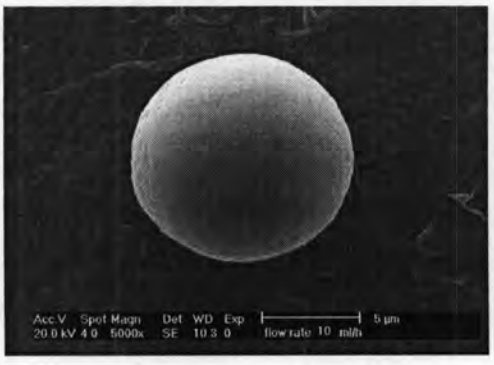

(b)

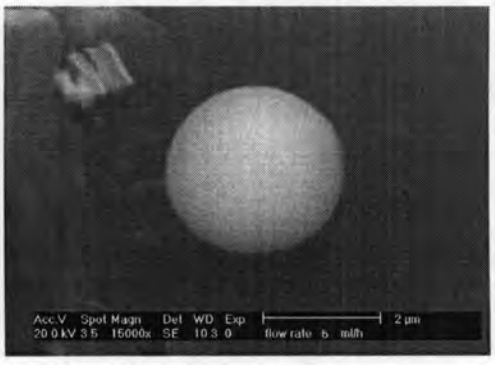

(c)

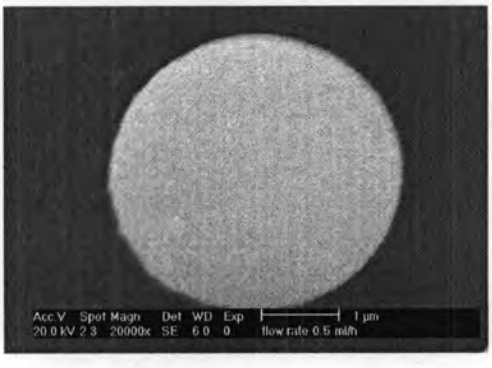

Figure 4.4 Effect of flow rate on size measured by SEM (a) 10 mL/h (b) 5 mL/h (c) 0.5 mL/h

Table 4.3 Effect of flow rate on particle size of chitosan

Flow rate (ml/h)	Shape	Size
0.5	Spherical microparticles	~2 μm
5	Spherical microparticles	~4 μm
10	Spherical microparticles	~8 μm

4.1.4 Effect of working distance

The influence of working distance (electrospraying distance) on the morphology and size of particles formed was studied. The effect of the working distance on the chitosan particle size was evaluated at 8, 10 and 12 cm, while maintaining the needle gauge, applied voltage, flow rate and stirring rate constant at 26 g, 13 kV, 10 mL/h and 400 rpm, respectively. Experiments were not conducted at distance lower than 8 cm, as such small distance lead to electric discharge. The solvent did not get enough time to evaporate completely before reaching the collector. Thus, these wet particles physically cross linked when they came in contact with each other on the collector, leading to aggregates of the particles. At the initial working distance of 8 cm, the particle size was 200 nm (figure 4.5 a). While, at working distance of 10 and 12 cm that were 500 and 1500 nm (figure 4.5 b-c).

Therefore, at a working distance of 8 cm, the chitosan spherical particle size was smaller than those obtained at 10 and 12 cm, due to the increase in the electric field strength, which in effect raises the rate of particle formation and leads to smaller a spherical size. Whereas, at the working distance of 12 cm, the electric field strength is decreased, which reduces the rate of sphere formation and leads to larger sized spherical particles. Thus, a working distance of 8 cm was selected as the working distance for subsequent experiments.

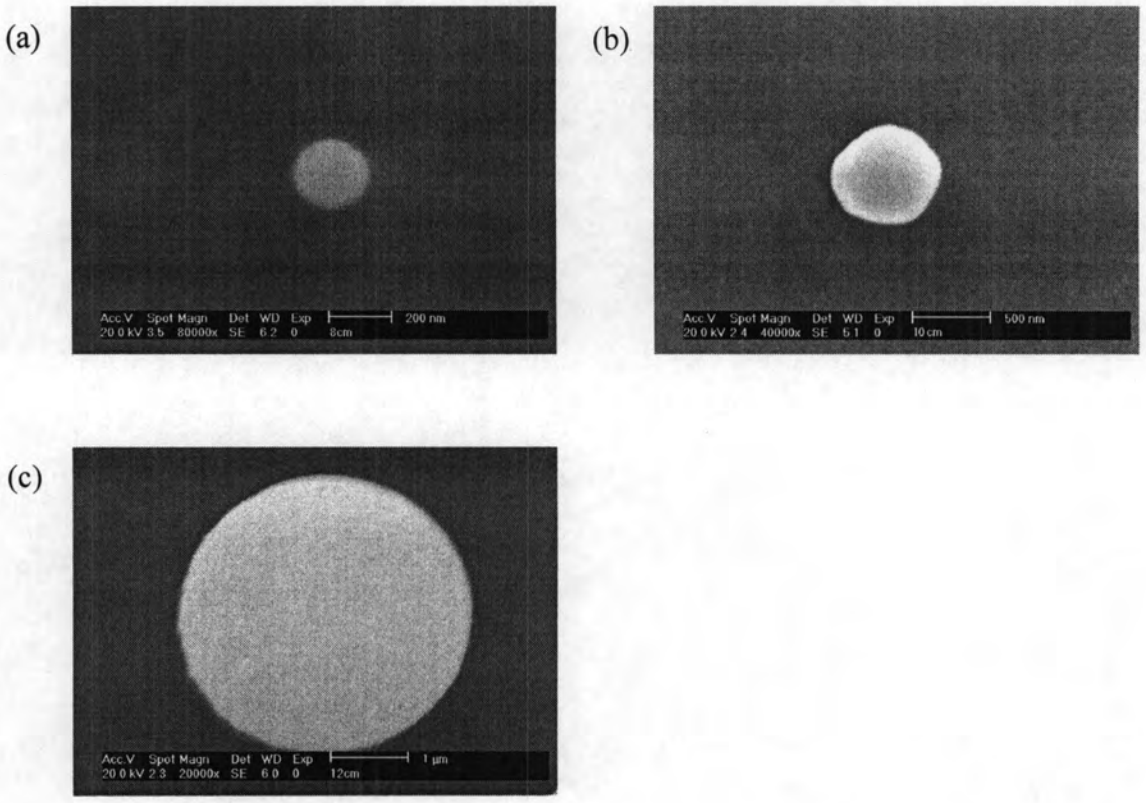

Figure 4.5 Effect of working distance on size measured by SEM (a) 8 cm (b) 10 cm (c) 12 cm

Table 4.4 Effect of working distance on particle size of chitosan

Working distance (cm)	Shape	Size
8	Spherical microparticles	~200 nm
10	Spherical microparticles	~500 nm
12	Spherical microparticles	~2 μm

An attempt was made in the present investigation to use biodegradable polymer in controlling the release of doxorubicin. In addition, the effort has increasingly become important in the formulation of pharmaceuticals from the polymer which includes chitosan, 4-carboxybenzenesulfonamide-chitosan and other polymer matrix.

4.2 Effect of pure polymer with DOX

4.2.1 Doxorubicin loaded chitosan and 4-carboxybenzenesulfonamide-chitosan nanoparticles

DOX loaded chitosan or 4-carboxybenzenesulfonamide nanoparticles were prepared by the electrospray ionization technique. The results from the preliminary studies of electrospray parameters on the nanoparticle sizes showed that the CS-DOX and m-CS-DOX nanoparticles were successfully prepared using electrospray parameters as follows: working distance of 8 cm, needle gauge of 26 g, flow rate of 0.5 ml/h, stirring rate of 400 rpm and electrospraying voltage of 13 kV.

4.2.2 Characterization of CS and m-CS with and without DOX nanoparticles

4.2.2.1 Morphology

Representative scanning electron micrographs (SEM) of CS and m-CS nanoparticles and their surface morphology were shown in Figure 4.6, the majority of the particles were in a uniform spherical shape with smooth surfaces and without visible pores. The surface of CS and m-CS could be clearly seen at high magnification (Figure 4.6 b and 4.6 d respectively). The average particle size of CS and m-CS without drug were 220.9±18.2 and 266.1±25.8 nm, respectively (ANOVA, P= 9.05×10^{-4}). The CS-DOX nanoparticles with different percentages of DOX (Figure 4.6 e-g) have a similar morphology of CS nanoparticles. The size of CS and CS-DOX

nanoparticles increased approximately from 220.9 to 569.0 nm (ANOVA, $P= 9.67x10^{-34}$) with the increasing percentages of DOX (Table 4.5).

Table 4.5 Effect of composition on morphology of the and zeta potential produced by optimal condition

Formulation	Particle size[a] (nm ± SD)	Particle size[b] (nm ± SD)	PDI[c]	SPAN[d]	Zeta potential (mV± SD)
• CS	220.9±18.2	383.3±33.8	0.799±0.061	0.600±0.087	-18.90±1.70
• m-CS	266.1±25.8	412.1±23.1	0.686±0.025	0.481±0.052	-19.23±2.30
• CS-DOX 0.25%	304.9±18.3	527.3±16.6	0.668±0.012	0.618±0.075	-15.30±2.90
• CS-DOX 0.5%	395.0±30.8	774.0±45.8	0.692±0.027	0.629±0.025	-13.62±1.90
• CS-DOX 1.0%	596.0±52.4	873.0±24.9	0.823±0.015	0.641±0.023	-10.69±2.50

[a]Particle size measured by SEM

[b]Particles size measured by particle size analyzer

[c]Polydispersity index from particle sizer

[d]SPAN : polydispersity Index (mean ± SD)

(a)

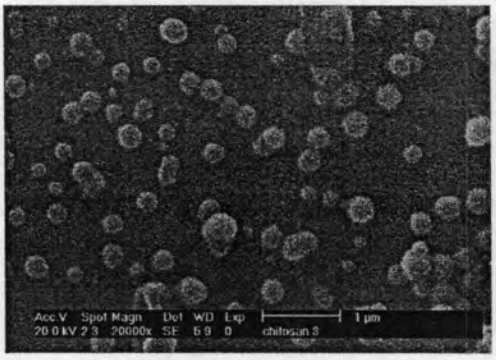
Acc.V Spot Magn Det WD Exp 1 µm
20.0 kV 2.3 20000x SE 5.9 0 chitosan 3

(b)

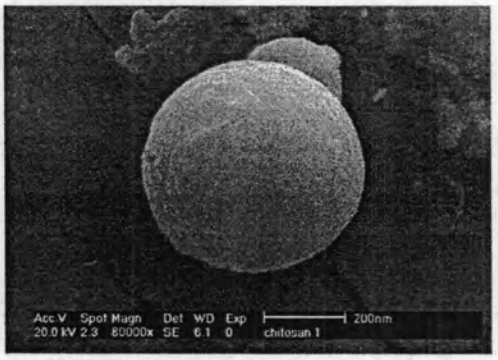
Acc.V Spot Magn Det WD Exp 200nm
20.0 kV 2.3 80000x SE 6.1 0 chitosan 1

(c)

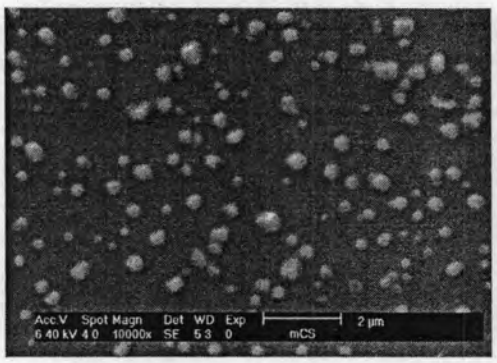
Acc.V Spot Magn Det WD Exp 2 µm
6.40 kV 4.0 10000x SE 5.3 0 mCS

(d)

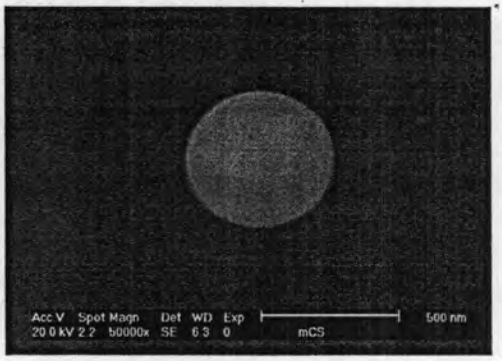
Acc.V Spot Magn Det WD Exp 500 nm
20.0 kV 2.2 50000x SE 6.3 0 mCS

(e)

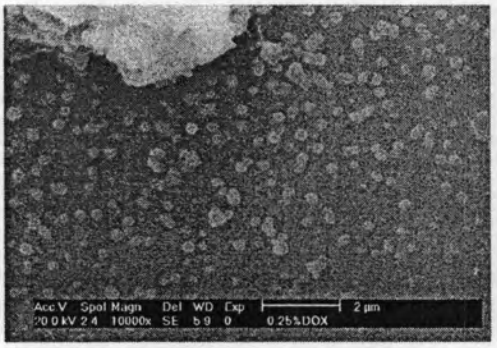
Acc.V Spot Magn Det WD Exp 2 µm
20.0 kV 2.4 10000x SE 5.9 0 0.25%DOX

(f)

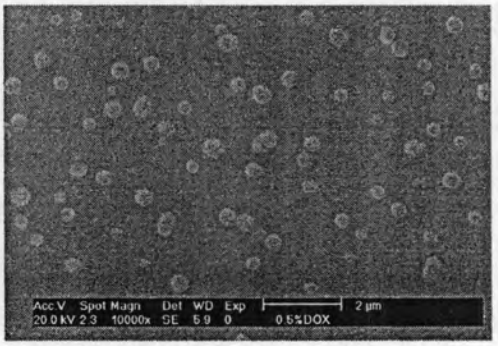
Acc.V Spot Magn Det WD Exp 2 µm
20.0 kV 2.3 10000x SE 5.9 0 0.5%DOX

(g)

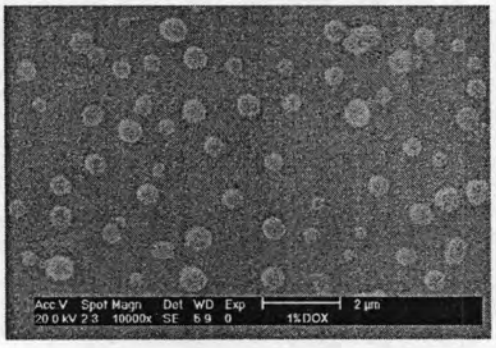
Acc.V Spot Magn Det WD Exp 2 µm
20.0 kV 2.3 10000x SE 5.9 0 1%DOX

Figure 4.6 SEM of particles (a) CS at wide screen, (b) CS (capture of one particle), (c) m-CS at wide screen, (d) m-CS (capture of one particle), (e) CS-DOX 0.25%, (f) CS-DOX 0.5%, (g) CS-DOX 1.0% at wide screen

4.2.2.2 Particle size and size distribution

The size distribution of CS and m-CS nanoparticles (Figure 4.7) were in approximately of 383.3 and 412.1 nm with the PDI approximately of 0.799 and 0.686 (ANOVA, P= 0.05) respectively. The size of m-CS was bigger than that of CS nanoparticles due to the viscosity of m-CS (36.7 cP) was higher than CS (10.9 cP). While SPAN values, as an indicator of particle size distribution were in approximately 0.600 and 0.481 respectively (Table 4.5). It was observed that the PDI and SPAN values of m-CS lower than that of CS.

The size distribution of CS and CS-DOX nanoparticles presented in Figure 4.8 showed that they were in the range approximately from 383.3-873.0 nm with PDI from 0.799 to 0.823 (Table 4.5), respectively. The size distribution of CS was narrower than that of the nanoparticles prepared from emulsion solvent evaporation [61]. In addition, when percentages of DOX increased it results in widely size distribution (Figure 4.8). While SPAN values, as an indicator of particle size distribution increased from 0.600 to 0.641 with an increase in the percentages of DOX. These results showed that the size distribution of nanoparticles is getting narrower with decreasing the ratios of DOX, because of the particle was separated as a stable form without the aggregation or slightly aggregation. A high value of SPAN indicates a wide distribution in size and a high polydispersity [62].

4.2.2.3 Zeta potential

When considering the zeta potential, that is surface charge, it can greatly influence particle stability in suspension through the electrostatic repulsion between particles [20]. The surfaces negative charge of CS and m-CS nanoparticles without DOX were -18.90 and -19.23 mV, respectively (Table 4.5) (n = 3, ANOVA, P = 0.84). The surface charge on droplet was negative because of the TPP effect.

Whereas, the surface charge of CS-DOX nanoparticles were decreased to -15.30 mV (n = 3, ANOVA, P = 0.05). The surface charge of CS-DOX nanoparticles with various ratios of DOX decreased from -15.3 to -10.6 mV when increasing the amount of DOX loaded amount (n = 3, ANOVA, P = 0.11).

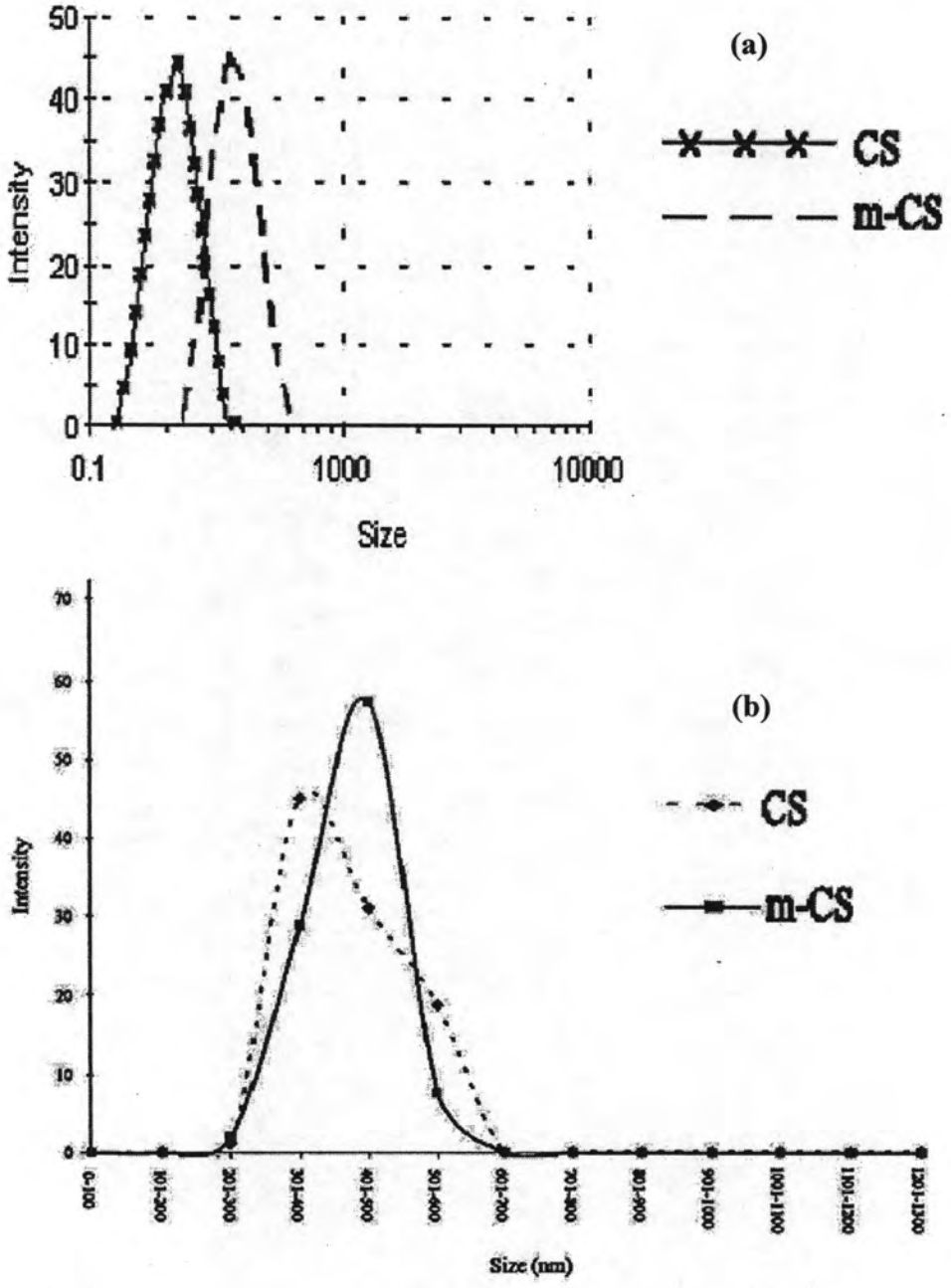

Figure 4.7 Size distribution of CS and m-CS nanoparticles (a) graph log, (b) graph divide by period of size

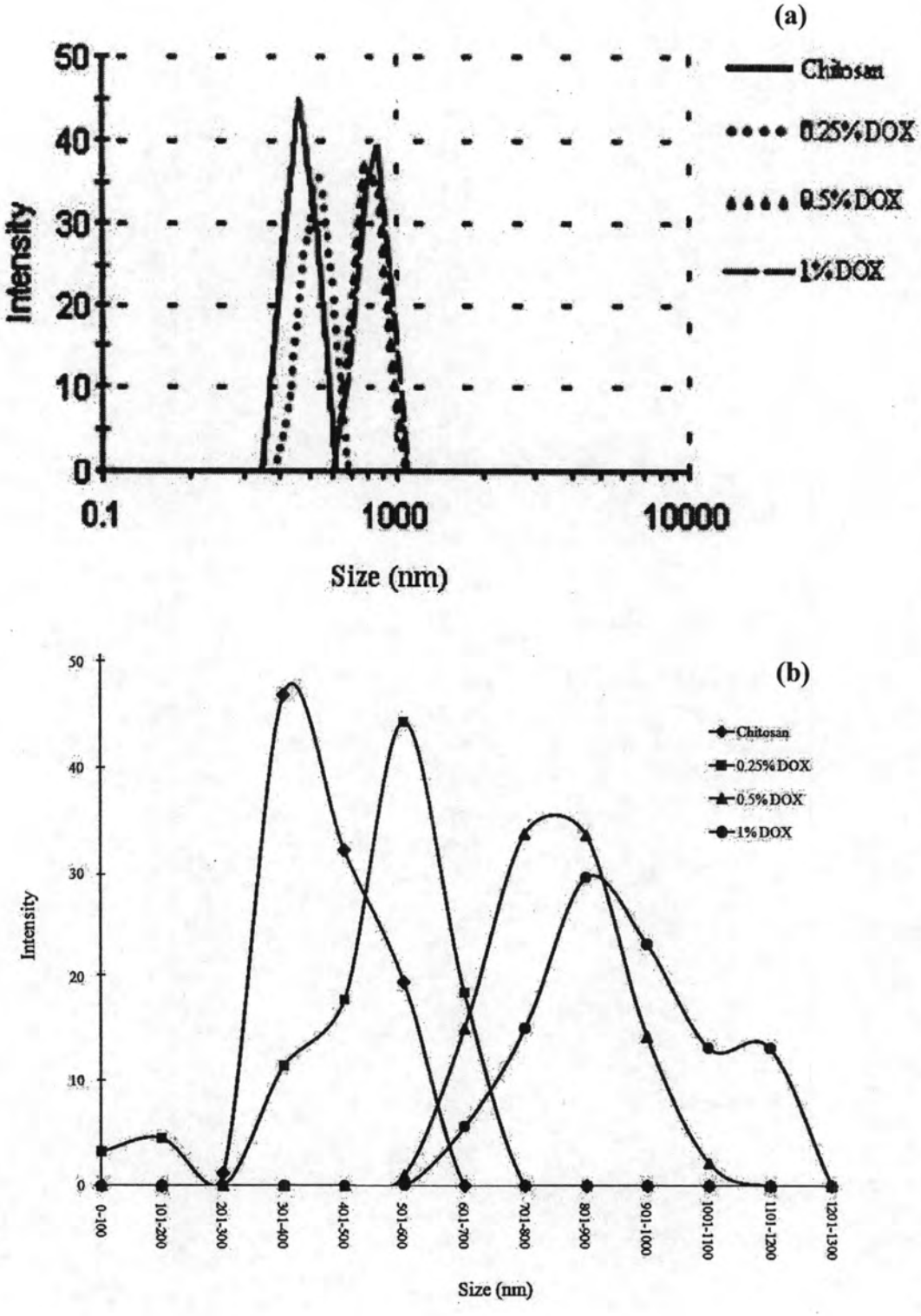

Figure 4.8 Size distribution of CS and CS-DOX nanoparticles (a) graph log, (b) graph divide by period of size

4.2.2.4 Fourier Transform Infrared Spectroscopy (FTIR)

FTIR spectroscopy was used to determine the chemical interaction of the CS and m-CS with the drug as displayed in Figures 4.9.

The FTIR spectrum of chitosan (Figure 4.9 a) showed a broad –OH and –NH stretch absorption band centered at 3440 cm^{-1}. The absorption band at 1657 and 1623 cm^{-1} were attributed to the amide of acetyl groups (O=C-NHR) and the N-H bending in chitosan. The absorption band at 1318 cm^{-1} resulted from combination of NH deformation and the –CN stretching vibration.

The FTIR spectrum of m-CS (4-CBS-CS) (Figure 4.9 b) showed the absorption peak at 1728 cm^{-1} corresponding to the C=O stretching of the modified chitosan. Peaks showed at 1653 and 1620 cm^{-1} were attributed to the amide of acetyl groups (O=C-NHR) and the N–H bending of unmodified chitosan. This was indicated that the unreacted CS was still remained in the product.

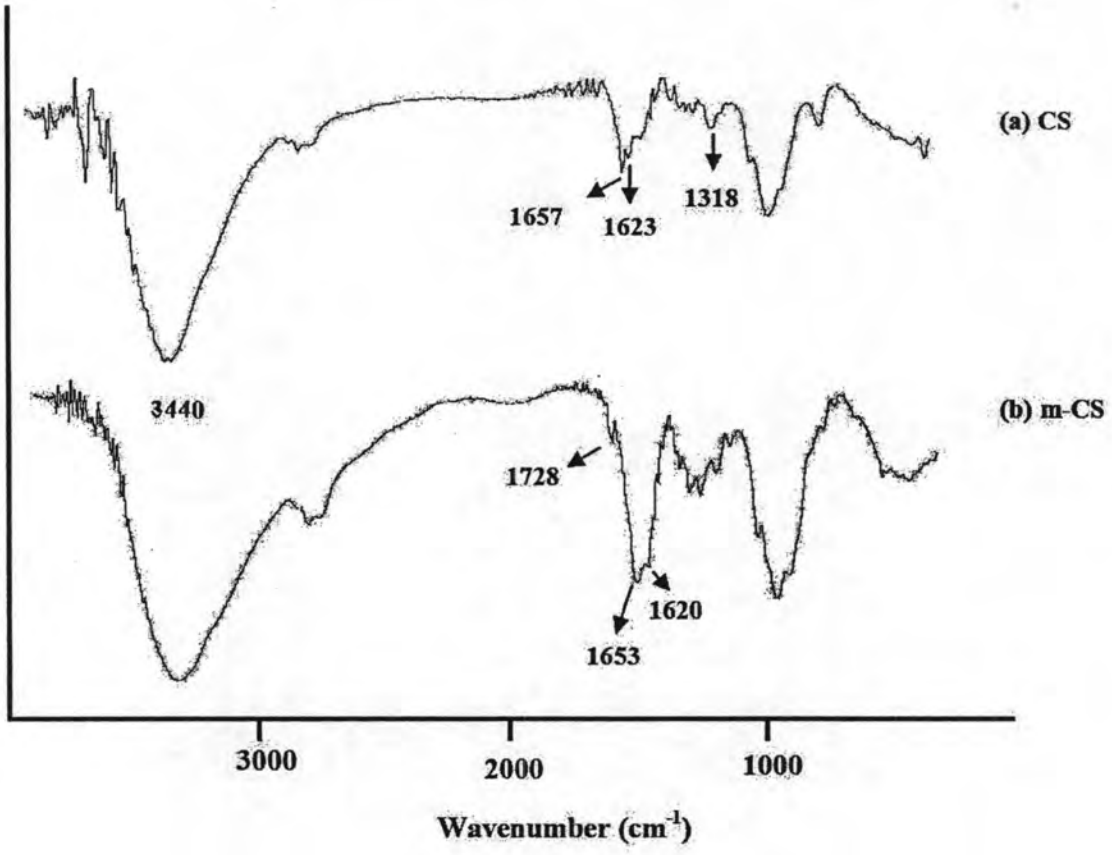

Figure 4.9 FTIR spectra of (a) CS, (b) m-CS

FTIR spectroscopy was used to determine the chemical interaction of chitosan and DOX (Figures 4.10).

The FTIR spectrum of doxorubicin (Figure 4.10 b) showed multiple peaks at 3432, 2925, 1725, 1623, 1407 and 1008 cm^{-1} corresponded to the different quinone and ketone carbonyl. However, it is difficult to indicate the different bands for the quinine and ketone because both compounds have carbonyl groups. The peak at 808 cm^{-1} was due to the stretching bands of C-O-CH_3.The peaks at 878 and 760 cm^{-1} were assigned to the amide I (–NH_2 wagging) and N–H deformation bonds.

The FTIR spectrum of CS-DOX nanoparticles with different ratio of DOX were shown in Figure 4.10 (c)-(e). In Figure 4.10 c, 0.25% DOX loaded CS, new absorption peaks presented at 1704 and 809 cm^{-1}, corresponding to the C-O-CH_3 stretching peaks of DOX, confirming the successful loading of DOX on CS nanoparticles. The FTIR spectra of another ratios are similar to that of 0.25% DOX loaded CS.

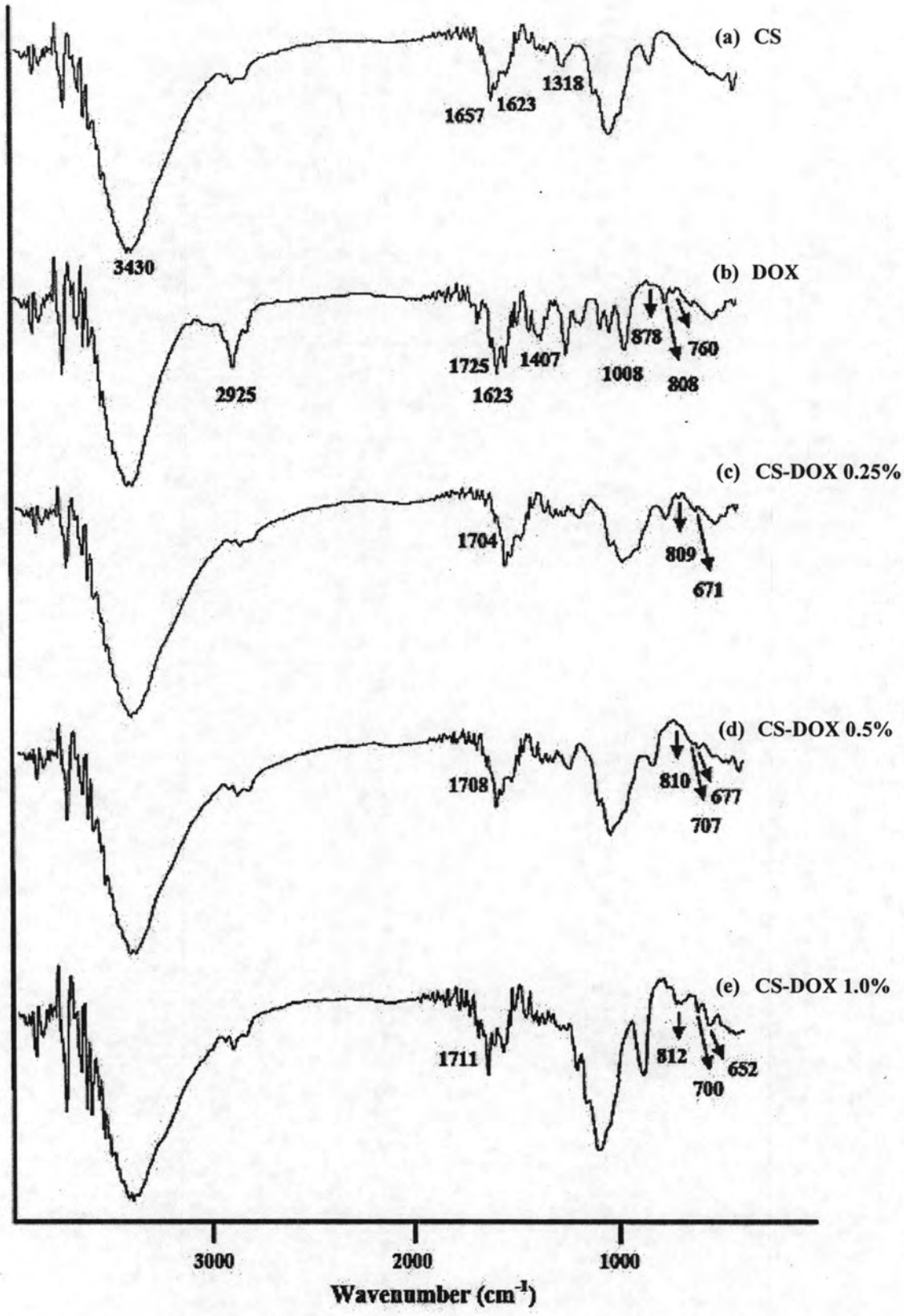

Figure 4.10 FT-IR spectra of (a) CS, (b) DOX, (c) CS-DOX 0.25%, (d) CS-DOX 0.5%, (e) CS-DOX 1.0%

4.2.2.5 Differential Scanning Calorimetry (DSC)

The DSC thermograms of the CS and m-CS nanoparticles were shown in Figure 4.11 (Perkin-Elmer DSC7, rate = 10 K/min).

The DSC thermogram of chitosan (CS), Figure 4.11a, showed an exothermic peak at 279°C which may be attributed to the decomposition of the chitosan.

The DSC thermogram of 4-carboxybenzenesulfonamide-chitosan (m-CS), Figure 4.11b, showed an endothermic peak at 232.1°C, indicating the melting temperature of 4-CBS. The exothermic peak at 283.0°C was assigned to a decomposition temperature of 4-CBS.

Therefore, the results confirmed that the chemical reactions of CS and 4-CBS resulted in new chemical bonds and hence new modified CS, contributing to the shifting of melting temperature.

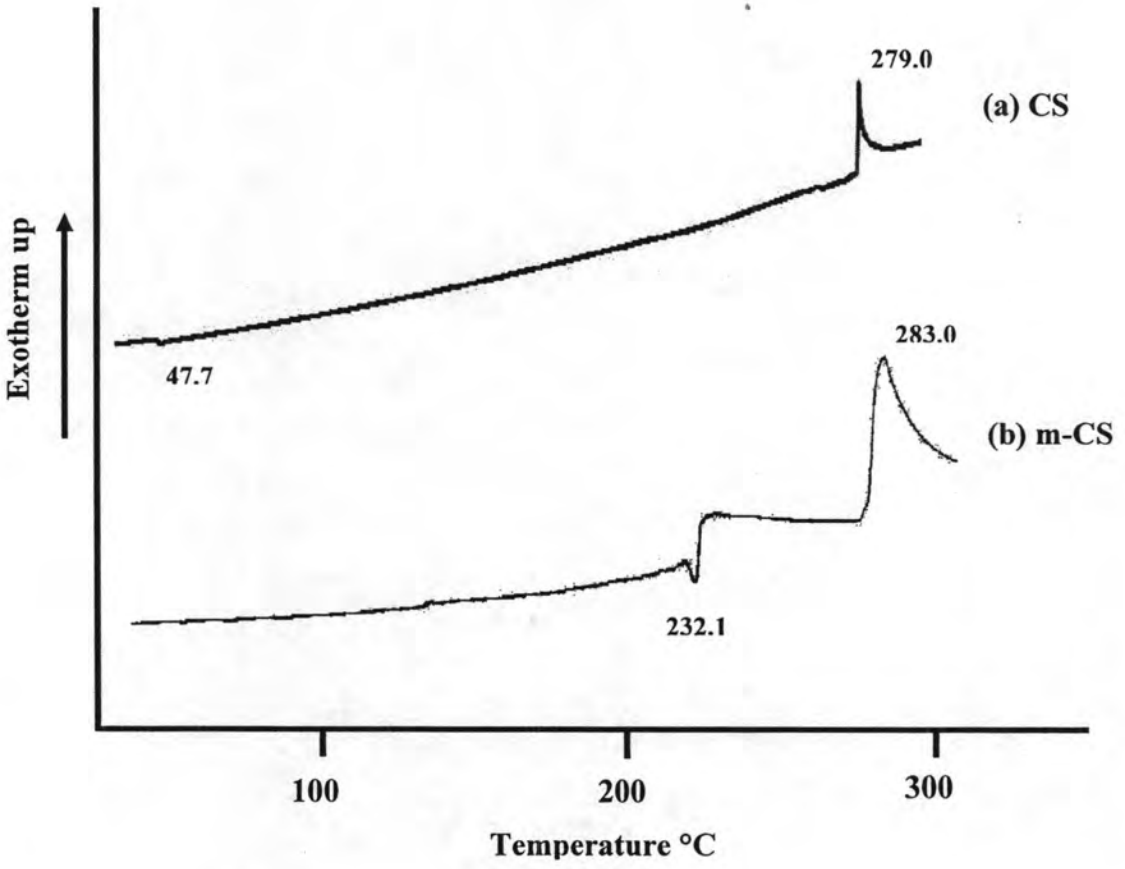

Figure 4.11 DSC thermograms of (a) CS and (b) m-CS nanoparticles

The DSC thermograms of the CS, CS-DOX (0.25%, 0.5% and 1.0%) nanoparticles were shown in Figure 4.12 (NETZSCH DSC7, rate = 10 K/min).

The CS nanoparticles thermogram revealed the endothermic broad peak around 117.17 °C, figure 4.12 a, which may be due to the loss of moisture content. Whereas the exothermic peak at about 279 °C. This peak represents the degradation of chitosan [63].

The DSC thermograms of the DOX loaded CS nanoparticles were displayed in Figure 4.12 (b)-(d). The thermogram of 0.25%DOX loaded CS nanoparticles (figure 4.12 b) showed an endothermic peak occurred at 118.83 °C which is higher than 117.17 °C of the pure CS, and endothermic peak at 193.17 °C indicating the melting temperature of pure doxorubicin DOX (T_m = 218 °C) [64]. The DSC thermograms of the another percentage of DOX loaded CS are similar to the one of the 0.25% DOX loaded CS nanoparticles.

Therefore, the DSC thermograms of the another loaded percentage of DOX loaded CS nanoparticles were similar in the shape and positions of the endothermic peaks. Thus, the DSC results showed that the interactions between CS and DOX were very small and did not significantly affect the thermal properties.

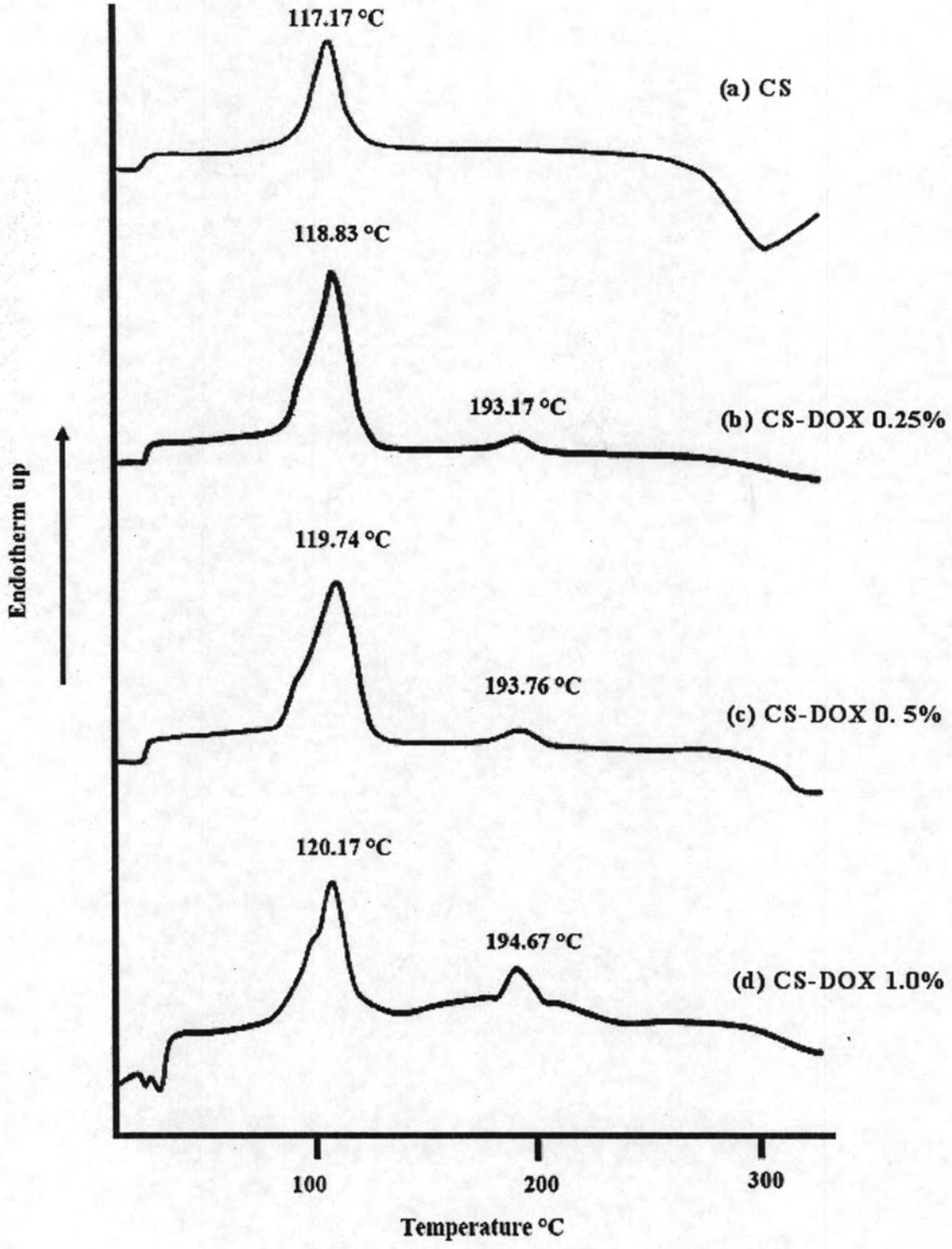

Figure 4.12 DSC thermograms of (a) CS, (b) CS-DOX 0.25%, (c) CS-DOX 0.5%, (d) CS-DOX 1.0%

4.2.2.6 Thermogravimetric analysis (TGA)

The TGA thermograms of the CS and m-CS nanoparticles were shown in Figure 4.13.

The TGA thermograms of CS (Figure 4.13 a) showed a weight loss of water about 5 % (30 °C to 150 °C). Afterwards, the degradation of CS occurred in the temperature range from 157 to 600 °C with the additional derivative thermogravimetric (DTG) peak at 298.4 °C and presented 45.6 % weight loss.

The TGA thermograms of m-CS (Figure 4.13 b) showed a weight loss of water about 14 % (30 °C to 180 °C). Afterwards, the degradation of m-CS occurred in the temperature range from 185 to 600 °C with the additional derivative thermogravimetric (DTG) peak at 290.3 °C and presented 55.7 % weight loss.

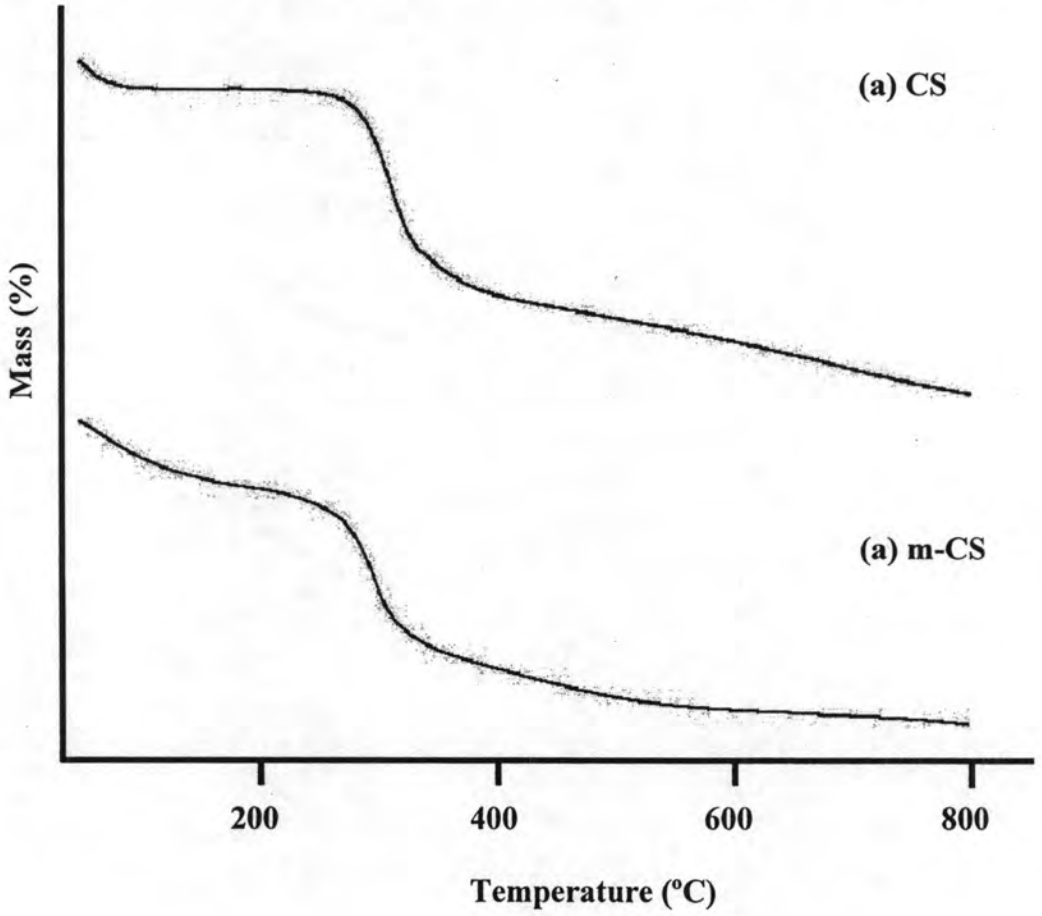

Figure 4.13 TGA thermograms of of (a) CS, (b) m-CS nanoparticles

The TGA thermograms of the 0.25%, 0.50% and 1.0% DOX loaded CS nanoparticles were shown in Figure 4.14.

The TGA thermograms of 0.25% DOX loaded CS (Figure 4.14 b) showed the combination of CS and DOX in 2 degradation stages. The thermogram of 0.25% DOX was shown a first stage range between 30 °C to 180 °C due to the loss of water. The second stage of weight loss starts at 200 °C to 270 °C during which there was 23.6 % weight loss with the DTG peak at 300.2 °C was due to the degradation of the CS. The different decreasing slope of TG curve indicated that there was no interaction between the CS nanoparticles and DOX. Furthermore, the weight loss temperature of the DOX-CS increased, when increasing the content of DOX onto CS nanoparticles. This might be attributed to DOX was entrapped by CS. The TGA thermograms of another percentages of DOX loaded CS (Figure 4.14 c-d) are similar to 0.25% DOX loaded CS.

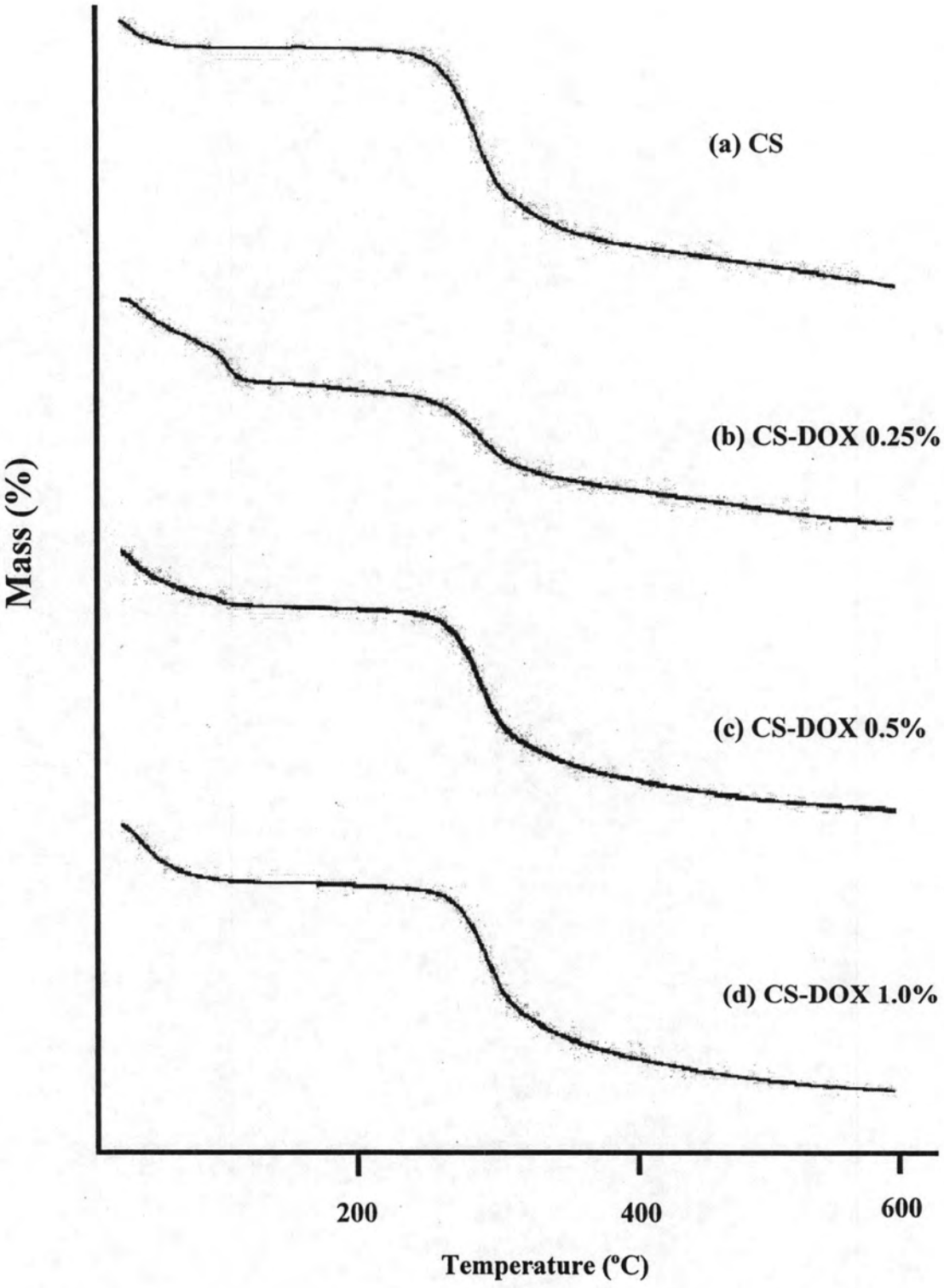

Figure 4.14 TGA thermograms of (a) CS, (b) CS-DOX 0.25%, (c) CS-DOX 0.5%, (d) CS-DOX 1.0%

4.2.3 Evaluation of drug encapsulation efficiency (%EE)

The percentages of encapsulation efficiency (%EE) of the DOX loaded CS and m-CS nanaoparticles were given in Table 4.6.

The encapsulation efficiency of drug within DOX loaded CS and m-CS nanaoparticles were analyzed using UV/Vis microplate reader spectroscopy at λ_{max} = 480 nm.

Generally, nanoparticles can entrap only small amounts of drug (9.1%) [2]. Therefore, in this work, the effect of DOX loading amount on encapsulation efficiency was investigated to achieve the higher percentage of encapsulation efficiency. The encapsulation efficiency of nanoparticless with 0.25%, 0.5%, and 1.0% DOX loaded CS were not significant (62.6% to 67.9%) respectively (Table 4.6) (ANOVA, $P = 0.46$).

This result indicated that the electrospray technique could produce higher percentage encapsulation up to 60% encapsulation.

Table 4.6 Encapsulation and loading capacity of doxorubicin loaded polymer nanoparticles*

Formulations	% Encapsulation
• CS-DOX 0.25%	67.9 ± 5.5
• CS-DOX 0. 5%	62.6 ± 0.7
• CS-DOX 1.0%	63.4 ± 6.9
• m-CS-DOX 0.25%	72.4 ± 3.7

* mean ± SD (n=3)

4.2.4 *In vitro* DOX release profiles

4.2.4.1 Effect of amount DOX loaded CS

The releases of DOX can be described as a graph to explain the drug released profiles from the nanoparticles. The release rate of DOX loaded CS was given in Appendix B.

The *in vitro* release profiles of 0.25%, 0.5% and 1.0% DOX loaded CS nanoparticles were investigated in phosphate buffer solution (PBS, pH 7.4) until 100% of the drug was released (Figure 4.15). The cumulative release profiles of the 0.25% and 0.5% DOX loaded CS showed that about 50% of drug was released in 10 hours and DOX was still sustained released. The release profiles of the 1.0% DOX loaded CS showed the initial burst release in early stage. The burst release (within 3 hours) was considered to be due to the presence of more free drugs on the particle surface and larger diffusion area of the nanoparticles [65]. Moreover, about 50% of drug was released within the first 7 hours and the release rate of DOX was sustained.

It can be implied that CS can prolong release of DOX only 3 days. However, the aim to develop a preferred controlled release anticancer drug is that the drug should be released for a long period of time, for example, more than 30 days. Therefore, the new polymer was chosen for further studies to improve the prolonged-release profile.

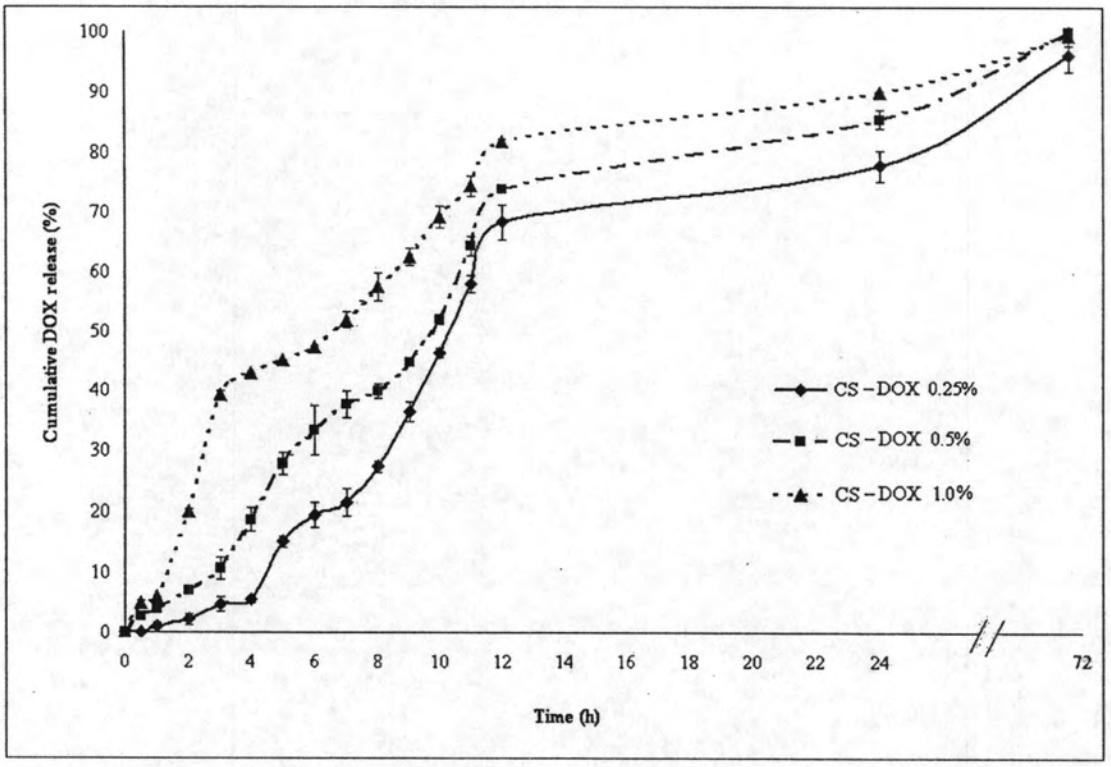

Figure 4.15 Release profiles of doxorubicin (DOX) from chitosan nanoparticles at pH 7.4, 37°C (average± SD, n=3)

4.2.4.2 Effect of DOX loaded m-CS

The comparison of the release profiles of DOX loaded CS and m-CS as a function of time for 10 days was given in Figure 4.61 and Appendix B. The release profiles of the DOX loaded CS as reported above showed burst effect of nearly 60% released after 24 hours in pH 7.4 buffer, and then followed by sustained release during the 6 days faster than the target goal of 30 days. The burst release (within 3 hours) was considered to be due to the presence of more free drugs on the particle surface and larger diffusion area of the nanoparticles [65]. Therefore, to archive the target goal, m-CS was used.

The DOX loaded m-CS nanoparticles could reduce the burst release at the beginning stage, only 30% was burst released in 8 hours and then followed by the sustained release of DOX. About 50% of drug was released in 2 days which was longer than that of DOX loaded CS (50% release after 48 hours) and DOX was sustained released until archived 100% within 10 days, which was longer than that from DOX loaded CS (6 days) .

This result can be implied that m-CS can prolong release of DOX more than CS. Therefore, the m-CS was selected for further studies to prolong the release rate.

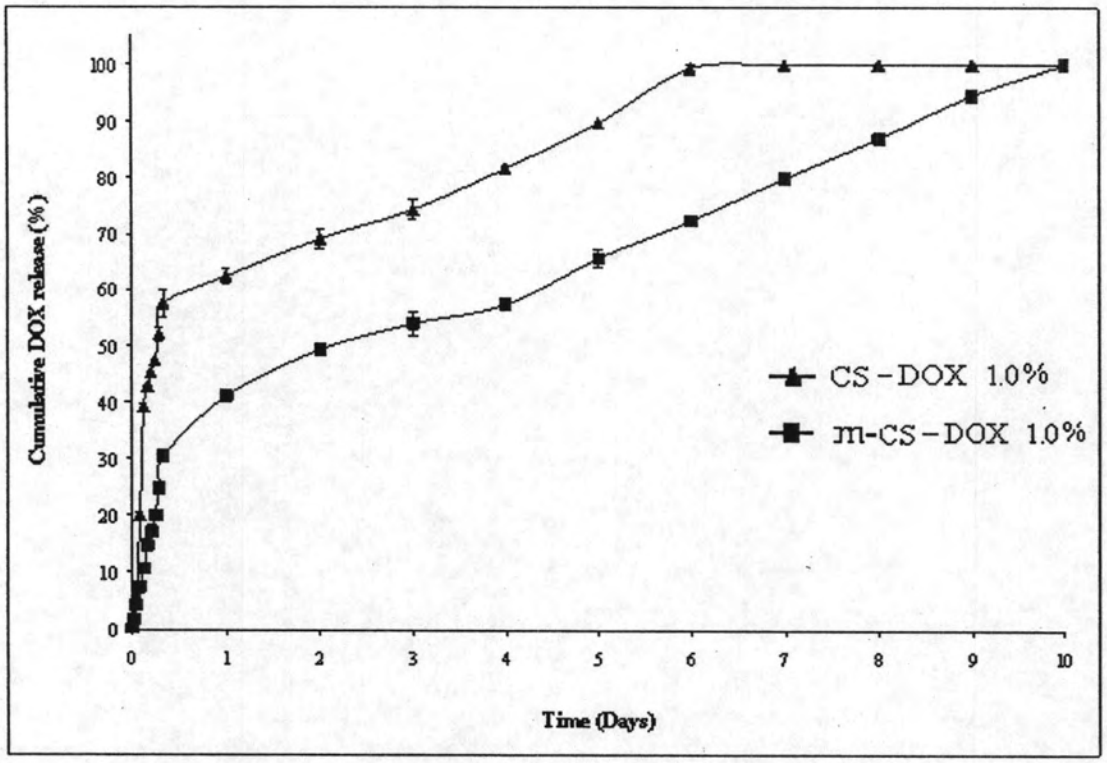

Figure 4.16 Release of doxorubicin (DOX) from CS and m-CS nanoparticles at pH 7.4, 37°C (average± SD, n=3)

4.3 Effect of anionic and cationic copolymer matrix of m-CS with DOX

The DOX could be prolonged released from the m-CS nanoparticles within 10 days. To improve the prolong release profile of DOX, the anionic and cationic copolymer matrix of m-CS and the other polymer was investigated. Alginate (Alg) and chitosan (CS) were used as a representative of anionic and cationic polymers, respectively. Therefore, the nanoparticles of m-CS/CS and m-CS/Alg copolymer matrix were investigated.

4.3.1 Morphology

Representative scanning electron micrographs (SEM) of m-CS/CS and m-CS/Alg nanoparticles and their surface morphology were shown in Figure 4.17, the majority of the particles were in a uniform spherical shape with smooth surfaces and without visible pores. The average particles size of m-CS/CS and m-CS/Alg were 324.6±16.3 and 243.1±17.8 nm, respectively

(a) (b)

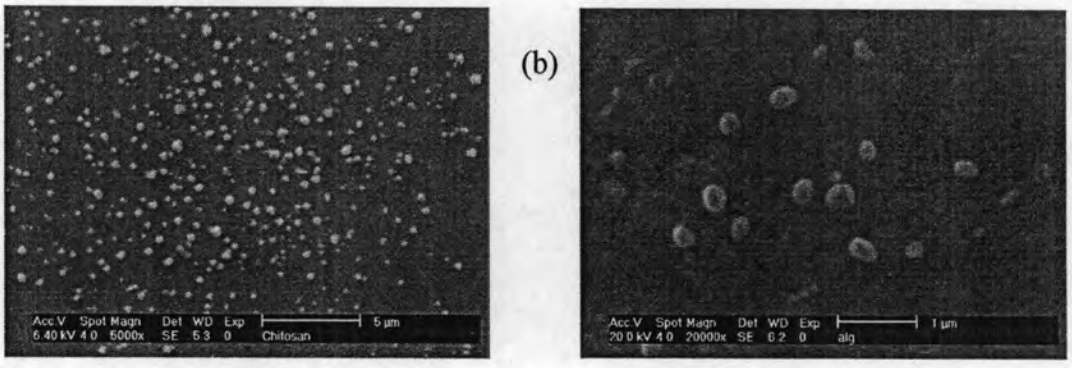

Figure 4.17 SEM of particles (a) m-CS/CS, (b) m-CS/Alg nanoparticles

4.3.2 *In vitro* DOX release profiles

The releases of DOX can be described as a graph to explain the drug release profile from the nanoparticles as a function of time in pH 7.4 buffer. The release

amounts of DOX from m-CS/CS and m-CS/Alg nanoparticles are given in Appendix B.

The *in vitro* release profiles of 1.0% DOX loaded m-CS/CS and m-CS/Alg nanoparticles were investigated in phosphate buffer solution (PBS, pH 7.4) for 15 days (Figure 4.18). The cumulative release showed that the 1.0% DOX loaded m-CS/Alg was prolonged release longer than that from the m-CS/CS (10 days vs. 6 days, respectively). The m-CS/Alg nanoparticles could reduced the burst effect as could be seen from only 10% was release at 7 hour. Moreover, about 50% of drug was released within 6 days which is longer than that from m-CS/CS (4 days) and followed by the sustained released rate.It can be implied that m-CS/Alg could prolonged release of DOX until 15 days. Therefore, an anionic polymer is an option for further studies to copolymer with m-CS to improve the prolonged release profile.

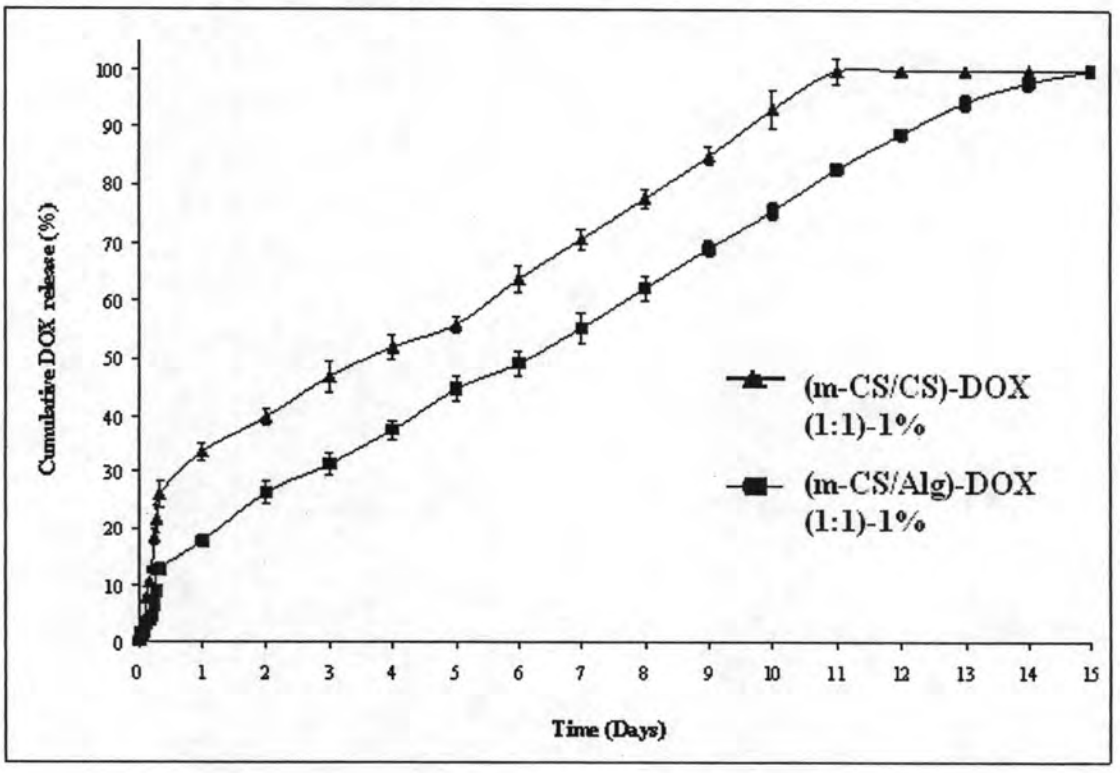

Figure 4.18 Release of doxorubicin (DOX) from m-CS/CS and m-CS/Alg nanoparticles at pH 7.4, 37°C (average± SD, n=3)

4.4 Effect of anionic copolymer matrix of CS and m-CS with DOX

The above results of release profiles revealed that the DOX loaded m-CS/Alg produced the most prolong release profile of 15 days, which Alg is a representative of anionic polymer. Thus, the PLA, anionic polymer, was chosen to study as a copolymer matrix with m-CS for controlling drug release.

In case of using PLA as a copolymer matrix with CS and m-CS, CS must be prepared in the form of hydropobic chitosan to improve the compatibility with PLA by modified with sodium dodecyl sulfate (HB-CS).

4.4.1 Hydrophobic chitosan (sodium dodecyl sulfate–chitosan complex) mixed poly (lactic acid)

4.4.1.1 Fourier transform infrared spectroscopy (FTIR)

FTIR spectroscopy was used to determine the chemical interaction of chitosan (CS) and hydrophobic chitosan (HB-CS) as displayed in Figures 4.19

The FTIR spectrum of chitosan (Figure 4.19 a) showed a broad –OH and –NH stretch absorption band centered at 3440 cm^{-1}. The absorption band at 1657 and 1623cm^{-1} were attributed to the amide of acetyl groups (O=C-NHR) and the N-H bending in chitosan. The absorption band at 1318 cm^{-1} resulted from combination of NH deformation and the –CN stretching vibration.

The FTIR spectrum of hydrophobic chitosan (HB-CS) (Figure 4.19 b) showed a broad –OH stretching absorption band centered at 3440 cm^{-1}. However, the intensity of–OH stretching was decreased. The paeks at 585 and 632 cm were due to the presence of sodium dodecyl sulfate. They could be attributed to the vibration of the -SO which splits into these two peaks upon co-ordination to the Na^+ [66].

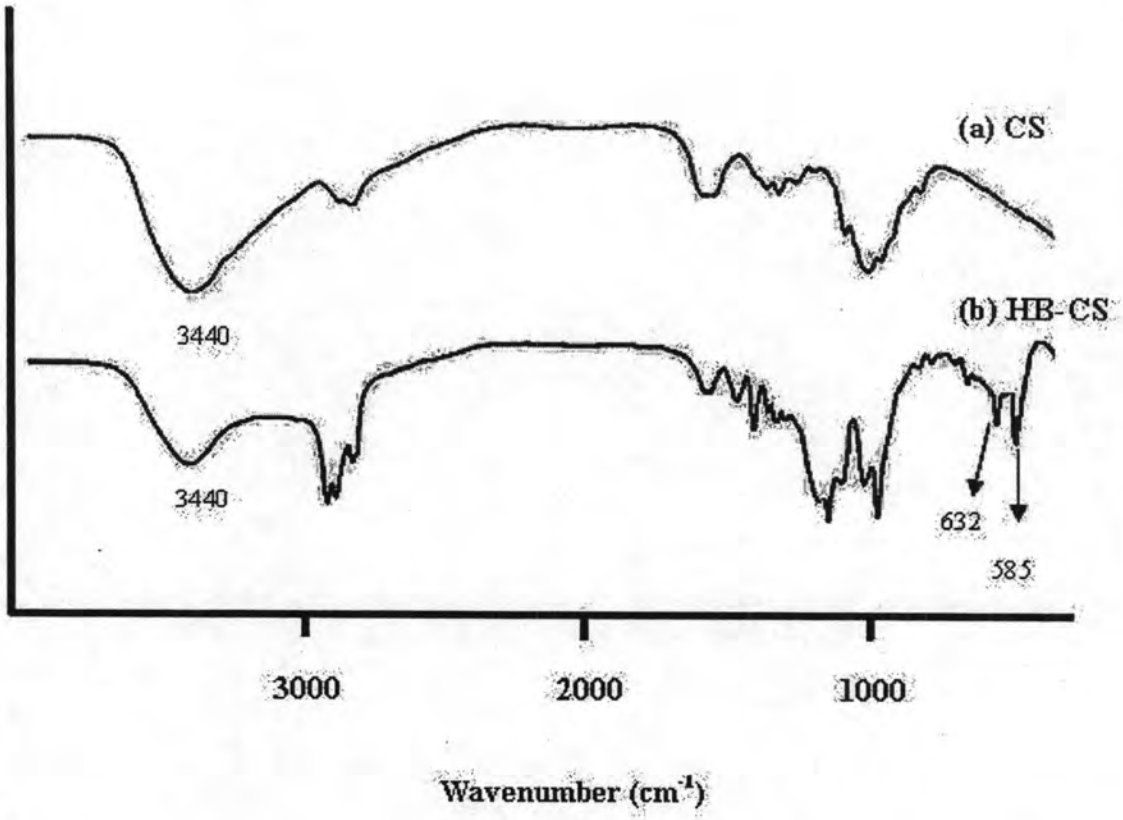

Figure 4.19 FTIR spectra of (a) CS, (b) HB-CS

4.4.1.2 Thermogravimetric analysis (TGA)

The TGA thermograms of CS and HB-CS were shown in Figure 4.20. The CS (Figure 4.20 a) showed a weight loss of water about 5 % (30 °C to 150 °C). Afterwards, the degradation of CS occurred in the temperature range from 157 to 600 °C with the additional derivative thermogravimetric (DTG) peak at 298.4 °C and presented 49.5 % weight loss.

The HB-CS (Figure 4.20 b) showed a weight loss of water about 2 % (30 °C to 150°C). Afterwards, the degradation of CS occurred in the temperature range from 157 to 600 °C with the additional derivative thermogravimetric (DTG) peak at 238.3 °C and presented 54.5 % weight loss.

The results showed that the degradation temperature of CS higher than HB-CS owing to CS chains having H-bonds while H-bonds of HB-CS were reduced by surfactant (SDS).

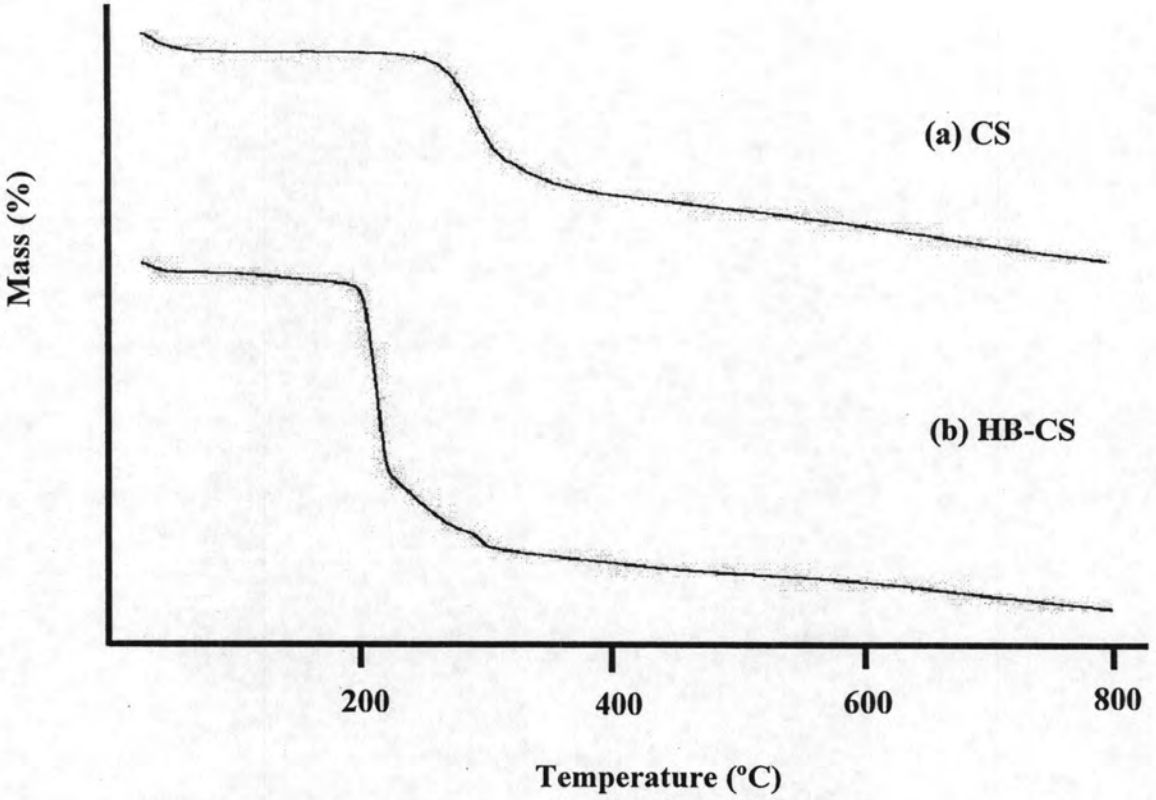

Figure 4.20 TGA thermograms of (a) CS, (b) HB-CS

4.4.1.3 Powder x-ray diffraction (XRD)

The X-ray powder diffraction patterns of CS and HB-CS showed in Figure 4.21.

The diffractogram of chitosan (Figure 4.21 a) showed two strong crystalline peaks at $2\theta = 10.4°$ and 21.8°, consistent with the previously reported by Lin [67].

The diffractogram of HB-CS (Figure 4.21 b) showed the board peaks at 2θ about 20.0^{o} with very low intensity, albeit at the same positions of the characteristic peaks of CS, implying that the crystallinity of CS was disrupted after being combined with SDS via electrostatic interactions.

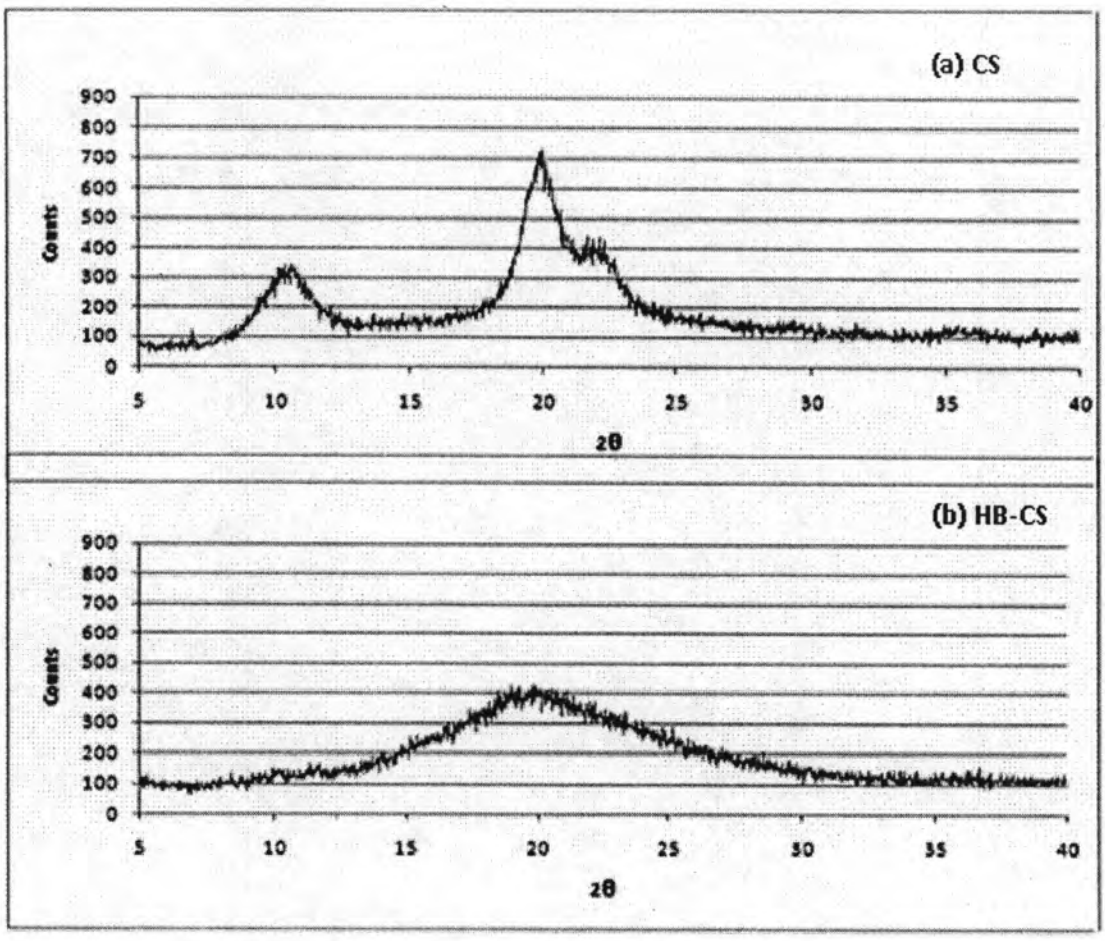

Figure 4.21 X-ray diffractograms of (a) CS, (b) HB-CS

4.4.2 Doxorubicin loaded chitosan and 4-carboxybenzenesulfonamide-chitosan mixed poly (lactic acid) nanoparticles

DOX loaded chitosan or 4- carboxybenzenesulfonamide chitosan nanoparticles mixed poly (lactic acid) were prepared by the electrospray ionization technique. The results from the preliminary studies of electrospray parameters on the nanoparticle sizes showed that the CS/PLA-DOX and m-CS/PLA-DOX nanoparticles were successfully prepared using electrospray parameters as follows: working distance of 8 cm, needle gauge of 20 g, flow rate of 10 ml/h, stirring rate of 800 rpm and electrospraying voltage of 10 kV.

4.4.3 Characterization of CS and m-CS mixed PLA with and without DOX nanoparticles

4.4.3.1 Morphology

Representative scanning electron micrographs (SEM) and their surface morphology of CS/PLA and m-CS/PLA nanoparticles were shown in Figure 4.22, the particles were in a uniform spherical shape with visible pores. The surface of CS and m-CS mixed PLA nanoparticles could be clearly seen at high magnification (Figure 4.22 b and 4.22 d, respectively). The average particles size of CS/PLA and m-CS/PLA were 159.4±19.6 and 227.8±38.8 nm, respectively (Table 4.7).

The morphology and their surface morphology of the (CS/PLA)-DOX and (m-CS/PLA)-DOX nanoparticles with various ratios of DOX were shown in Figure 4.22, the majority of the particles were a spherical form and devoid of aggregates. The obtained nanoparticles (Figure 4.22 e-i) have appeared spherical in shape and within nanometer range. The size of the particles were increased when increasing the ratio of m-CS (ANOVA, $P= 2.90x10^{-2}$). However, when increasing the PLA ratio, the paticle sized were decrease (ANOVA, $P= 7.93x10^{-5}$). Finally, the size of the particles increased with the increasing the ratio of DOX (ANOVA, $P= 1.05x\ 10^{-4}$) (Table 4.7).

Table 4.7 Effect of composition on morphology of the and zeta potential produced by optimal condition

Formulation	Particle size[a] (nm ± SD)	Particle size[b] (nm ± SD)	PDI[c]	SPAN[d]	Zeta potential (mV± SD)
• CS/PLA	159.4±19.6	307.5±12.3	0.569±0.032	0.305±0.041	-21.70±1.73
• m-CS/PLA	227.8±38.8	361.3±17.4	0.455±0.034	0.223±0.019	-22.57±0.76
• (CS/PLA)-DOX (1:1 w/w)-1%	184.9±23.7	365.3±20.4	0.560±0.036	0.512±0.014	-24.03±0.96
• (m-CS/PLA)-DOX (1:1 w/w)-1%	232.7±7.5	409.5±8.6	0.570±0.082	0.443±0.019	-31.50±0.96
• (m-CS/PLA)-DOX (2:1 w/w)-1%	250.2±10.1	437.2±13.7	0.645±0.035	0.498±0.017	-15.57±1.12
• (m-CS/PLA)-DOX (1:2 w/w)-1%	118.9±9.4	357.1±38.3	0.602±0.010	0.337±0.011	-17.07±0.74
• (m-CS/PLA)-DOX (1:2 w/w)-2%	278.1±15.3	406.6±11.4	0.705±0.016	0.582±0.014	-15.78±1.11

[a]Particle size measured by SEM [b]Particles size measured by particle size analyzer

[c]Polydispersity index from particle sizer [d]SPAN : polydispersity Index (mean ± SD)

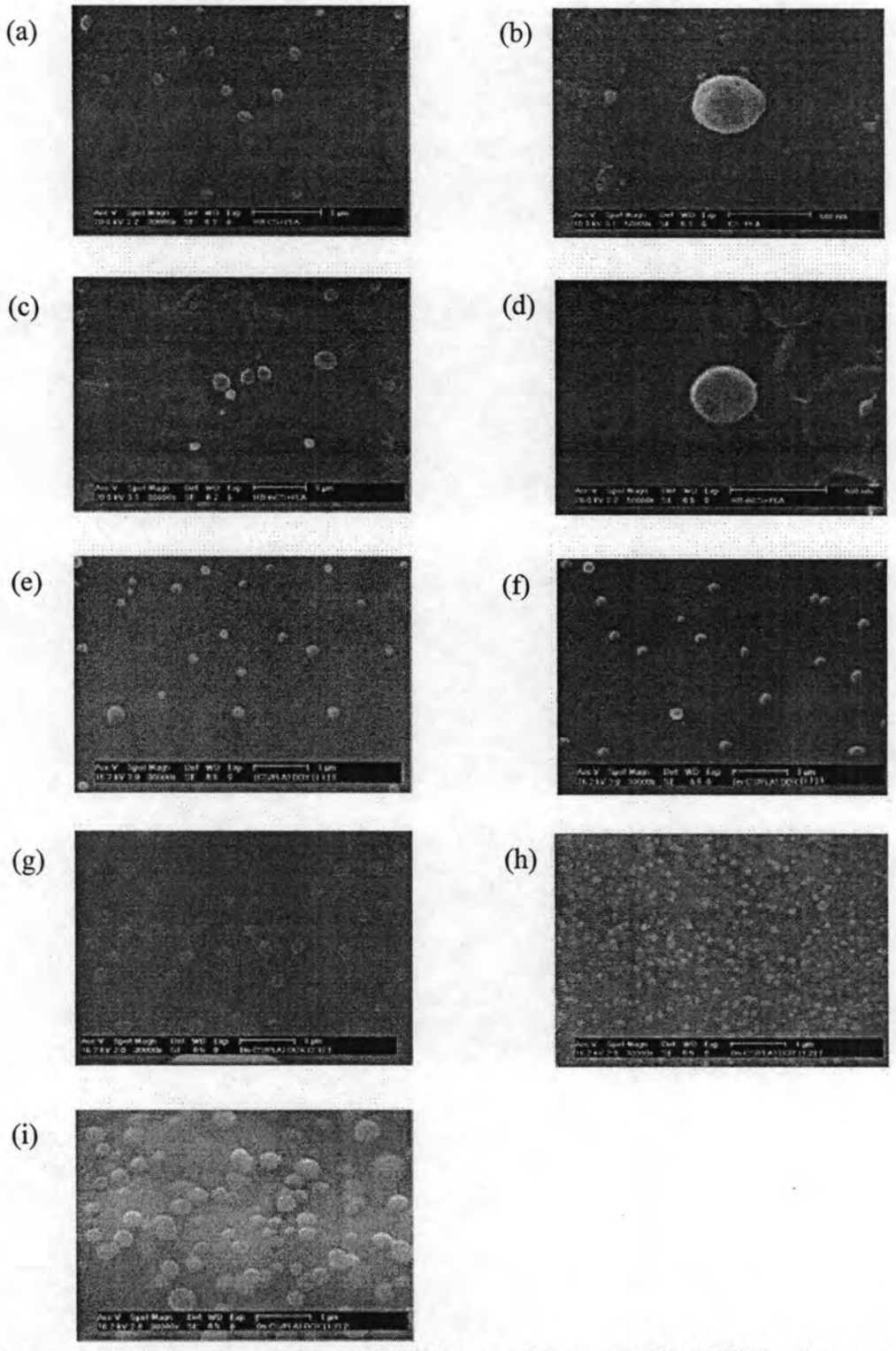

Figure 4.22 SEM of particles (a) CS/PLA at wide screen (b) CS/PLA (capture of one particle) (c) m-CS/PLA at wide screen (d) m-CS/PLA (capture of one particle) (e) (CS/PLA)-DOX (1:1 w/w)-1% (f) (m-CS/PLA)-DOX (1:1 w/w)-1% (g) (m-CS/PLA)-DOX (2:1 w/w)-1% (h) (m-CS/PLA)-:DOX (1:2 w/w)-1% (i) (m-CS/PLA)-DOX (1:2 w/w)-2%

4.4.3.2 Particle size and size distribution

The size distribution of CS/PLA and m-CS/PLA nanoparticles presented in Figure 4.23 showed that they were in approximately 307.5 and 361.3 nm with PDI approximately 0.569 and 0.455 respectively. It was observed that the size of m-CS/PLA larger than that of CS/PLA nanoparticles due to the viscosity of m-CS/PLA (2.80 cP) was higher than CS/PLA (10.41 cP). These results were consistent with the SPAN values of 0.305 and 0.223 respectively (Table 4.7). It was observed that both PDI and SPAN values of CS/PLA higher than that of m-CS/PLA.

The size distribution of (CS/PLA)-DOX (1:1 w/w)-1%, (m-CS/PLA)-DOX (1:1 w/w)-1%, (m-CS/PLA)-DOX (2:1 w/w)-1%, (m-CS/PLA)-DOX (1:2 w/w)-1% and (m-CS/PLA)-DOX (1:2 w/w)-2% nanoparticles presented in Figure 4.24 showed that they were in approximately 365.3, 409.5, 437.2 , 357.1 and 406.6 nm, respectively with PDI approximately 0.560, 0.570, 0.645, 0.602 and 0.705 respectively. While SPAN values, as an indicator of particle size distribution were in approximately 0.512, 0.443, 0.498, 0.337 and 0.582 respectively (Table 4.7). The results indicated that PDI and SPAN value increased when decreasing amount PLA and DOX.

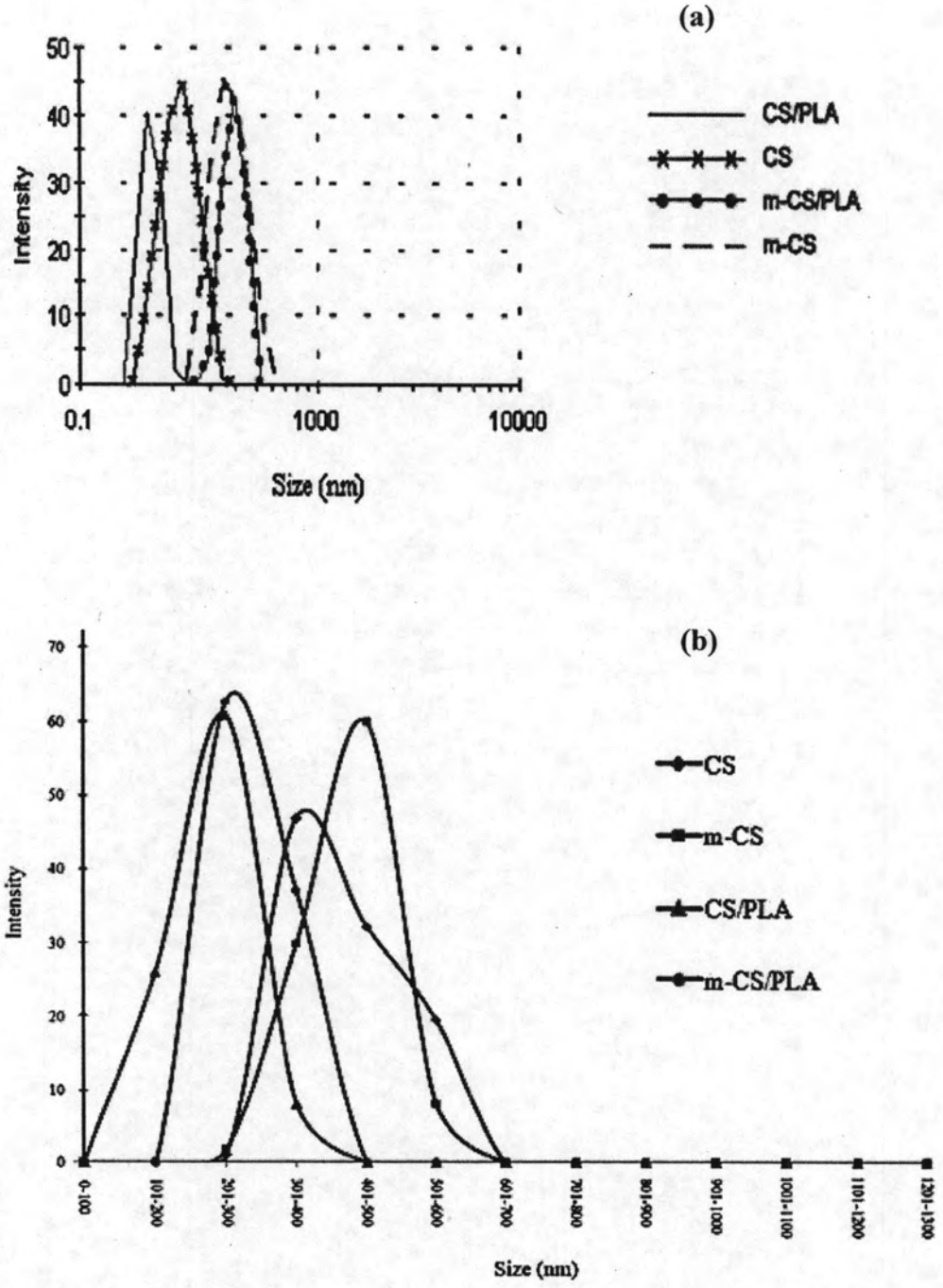

Figure 4.23 Size distribution of CS, m-CS, CS/PLA and m-CS/PLA nanoparticles (a) graph log, (b) graph divide by period of size

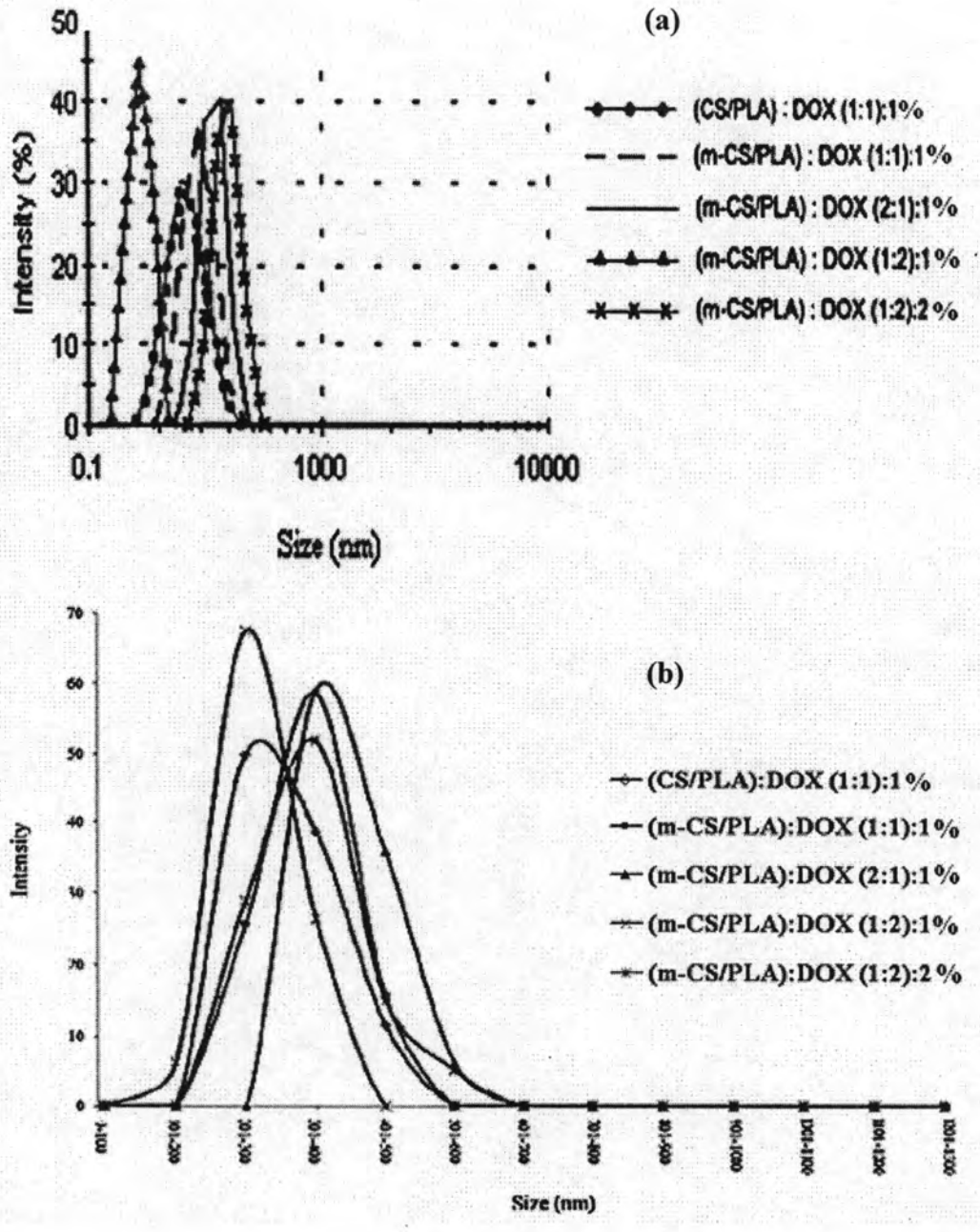

Figure 4.24 Size distribution of (CS/PLA):DOX (1:1 w/w)-1%, (m-CS/PLA):DOX (1:1 w/w)-1%, (m-CS/PLA):DOX (2:1 w/w)-1%, (m-CS/PLA):DOX (1:2 w/w)-1%, (m-CS/PLA):DOX (1:2 w/w)-2% nanoparticles (a) graph log (b) graph divide by period of size

4.4.3.3 Zeta potential

When considering the zeta potential, that is surface charge, it can greatly influence particle stability in suspension through the electrostatic repulsion between particles [20]. The surface of CS/PLA and m-CS/PLA nanoparticles have to possess negative charge of -18.90 and -19.23 mV, respectively (Table 4.7). The surface charge on droplet was negative because of effect of PLA and TPP. Whereas, the surface charge of CS/PLA and m-CS/PLA with 1% DOX nanoparticles (Table 4.7) were found to possess higher negative charge of -24.03 and -31.50 mV, respectively than that of without DOX (Table 4.7). When varying the ratio of CS, m-CS: PLA, the negative charge were reduced from the orginal 1:1 ratio with 1 DOX. However, with an increase in m-CS and PLA ratio, there was reduced surface charge of the particles (Table 4.7).

4.4.3.4 Fourier transform infrared spectroscopy (FTIR)

FTIR spectroscopy was used to determine the chemical interactions of CS or m-CS with PLA as displayed in Figures 4.25 -4.26.

4.4.3.4.1 Effect of presenting chitosan (CS) and m-chitosan (CS) with poly (lactic acid)

The FTIR spectrum of chitosan (Figure 4.25 a) showed a broad –OH and –NH stretch absorption band centered at 3440 cm^{-1}. The absorption band at 1657 and 1623cm^{-1} were attributed to the amide of acetyl groups (O=C-NHR) and the N-H bending in chitosan. The absorption band at 1318 cm^{-1} resulted from combination of NH deformation and the –CN stretching vibration.

The FTIR spectrum of m-CS (4-CBS-CS) (Figure 4.25 b) showed the absorption peak at 1728 cm^{-1} corresponding to the C=O stretching of the modified chitosan. A peak showed at 1620 cm^{-1} was attributed to N–H bending of unmodified chitosan, possibly indicating that there were still remained the unreacted CS in the product.

The FTIR spectrum of poly (lactic acid) (Figure 4.25 c) showed the strong C=O absorption peak at 1755 cm^{-1} and the absorption peak at 1180 cm^{-1} for C–O–C ester group proves the formation of –COO–.

The FTIR spectrum of CS/PLA (Figure 4.25 d) showed the absorption peak at 1620 cm^{-1} corresponding to N–H bending of amine (O=C-NHR) of chitosan and 1758 cm^{-1}, which represent the backbone ester group of poly (lactic acid).

The FTIR spectrum of m-CS/PLA (Figure 4.25 e) showed the absorption peak at 1729 ^{1} cm^{-1} corresponding to the C=O stretching of the modified chitosan and 1620 cm^{-1} was attributed to N–H bending of amine (O=C-NHR) of chitosan. A peak showed at 1760 cm^{-1}, which represent the backbone ester group of poly (lactic acid).

The FTIR spectrum of CS/PLA and m-CS/PLA (Figure 4.25 d-e) showed the characteristic peaks of chitosan, modified chitosan and poly (lactic acid) with no significantly shifts from the original positions of chitosan, m-chitosan and poly (lactic acid) before mixing. The peaks position of these spectra almost didn't change. It may be explained that the molecular interactions between chitosan, modified chitosan and poly (lactic acid) were weak because poly (lactic acid) does not have enough −OH groups to form hydrogen bonds with −OH groups and $-NH_2$ groups in chitosan.

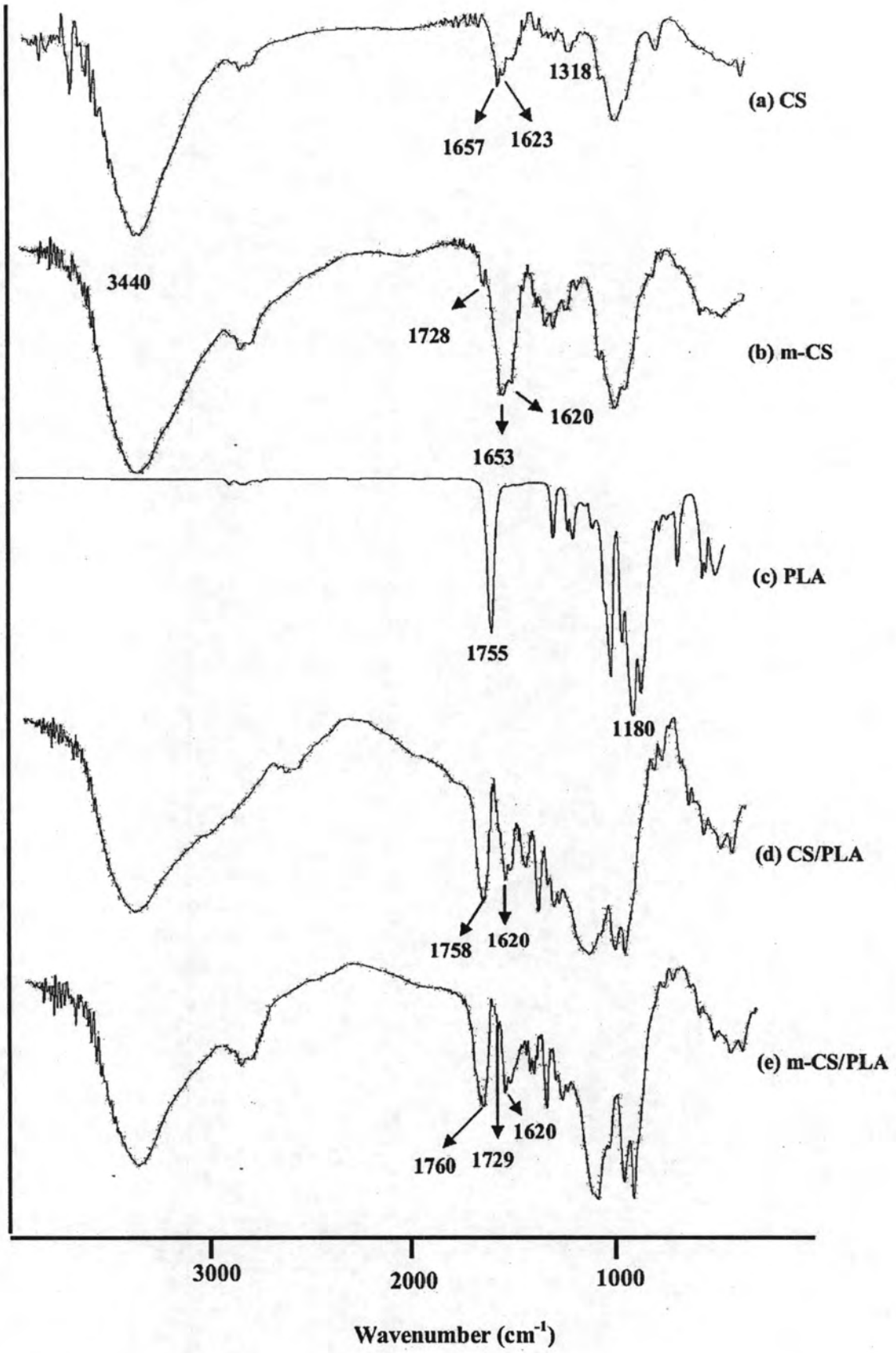

Figure 4.25 FT-IR spectra of (a) CS, (b) m-CS (c) PLA (d) CS/PLA (e) m-CS/PLA

4.4.3.4.2 Effect of presenting CS/PLA and m-CS/PLA with DOX

The FTIR spectrum of (CS/PLA)-DOX (1:1 w/w)-1% nanoparticles (Figure 4.26 e), there were additional absorption peaks at 815 cm^{-1} corresponding to the C-O-CH_3 stretching peaks and 870 and 739 cm^{-1} are due to the amide I (–NH_2) wagging and N–H deformation bonds of DOX, confirming the successful loading of DOX on the CS/PLA nanoparticles.

The FTIR spectrum of (m-CS/PLA)-DOX (1:1 w/w)-1% nanoparticles with different ratios (Figure 4.26 f-i). Obviously, with the increase of PLA, the relative strength of peak at 1758 cm^{-1} which belongs to carbonyl group in PLA was increased, and the relative strength of peak at 1657 and 1728 cm^{-1} which represent the amide I and C=O stretching absorption band of CS and m-CS, respectively was decreased. Moreover, there were additional absorption peaks at 808 cm^{-1} corresponding to the C-O-CH_3 stretching peaks and 874 and 758 cm^{-1} are due to the amide I (–NH_2) wagging and N–H deformation bonds of DOX, confirming the successful loading of DOX on the m-CS/PLA nanoparticles.

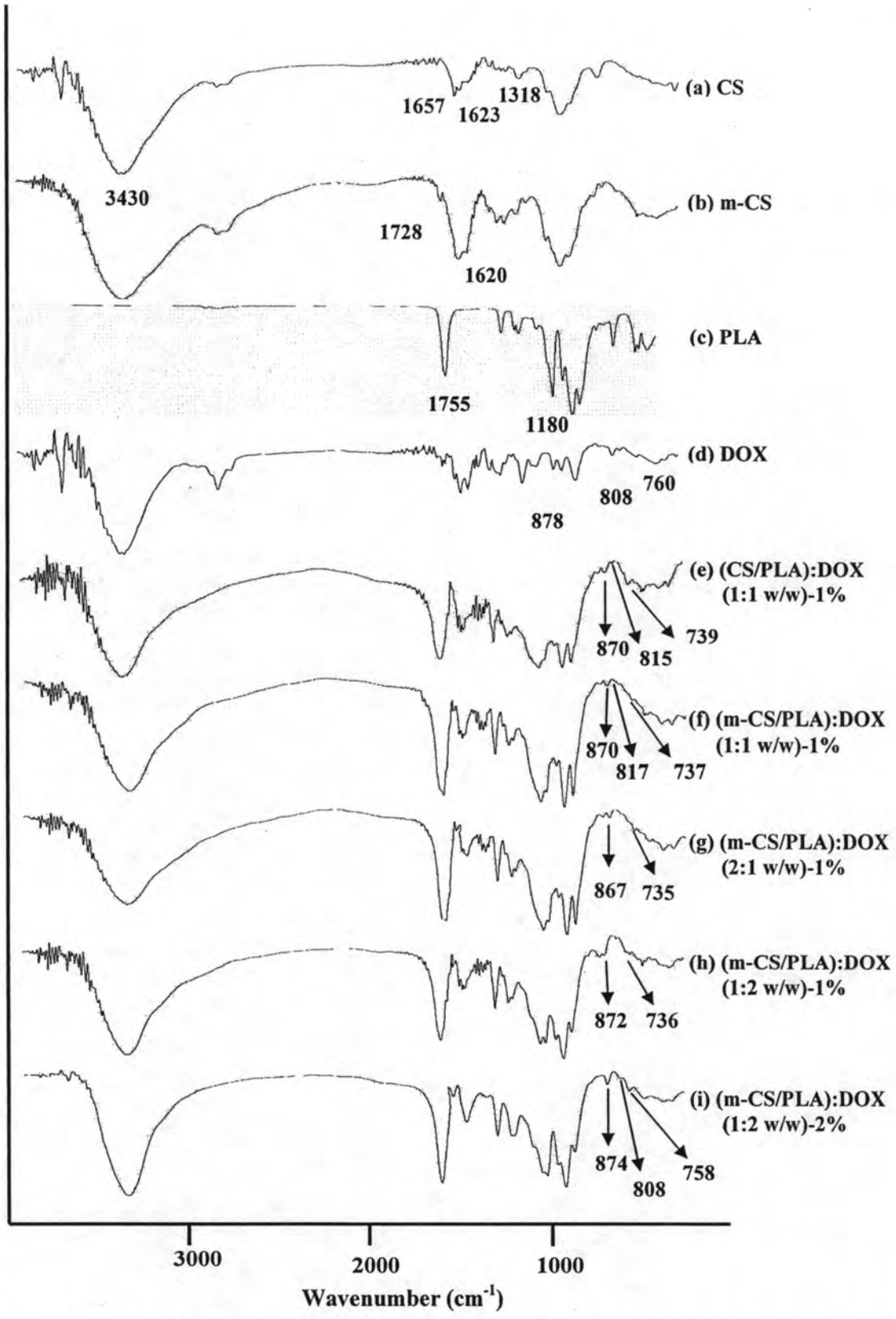

Figure 4.26 FTIR spectra of (a) CS, (b) m-CS, (c) PLA, (d) DOX, (e) (CS/PLA)-DOX (1:1 w/w)-1%, (f) (m-CS/PLA)-DOX (1:1 w/w)-1%, (g) (m-CS/PLA)-DOX (2:1 w/w)-1%, (h) (m-CS/PLA)-DOX (1:2 w/w)-1%, (i) (m-CS/PLA)-DOX (1:2 w/w)-2%

4.4.3.5 Differential Scanning Calorimetry (DSC)

4.4.3.5.1 Effect of presenting chitosan (CS) and m-chitosan (CS) with poly (lactic acid)

The DSC thermograms of the CS, m-CS, PLA, CS/PLA and m-CS/PLA nanoparticles were shown in Figure 4.27(Perkin-Elmer DSC7, rate = 10 K/min).

The DSC thermogram of chitosan (CS), (Figure 4.27 a), revealed a small endothermic transition at 47.7 °C which may be due to the loss of moisture content in the polysaccharide. There is an exothermic peak at 279.0°C which may be attributed to the decomposition of the chitosan.

The DSC thermogram of 4-carboxybenzenesulfonamide-chitosan (m-CS), (Figure 4.27 b), revealed an endothermic peak at 232.1°C, indicating the melting temperature of 4-CBS. The exothermic peak was shown at 283.0°C, which is a decomposition temperature of 4-CBS.

The DSC thermogram of poly (lactic acid) (PLA), (Figure 4.27 c), revealed a small glass transition at 50.2 °C and the melting endothermic peak at 162.1°C, which represented the melting temperature.

The DSC thermogram of CS/PLA, (Figure 4.27 d), revealed a small glass transition at 49.2 °C. The endothermic peak was shown at 180.2 °C may be related to the melting temperature of PLA. The exothermic peak at 246.0 °C may be related to the degradation of CS/PLA.

The DSC thermogram of m-CS/PLA, (Figure 4.27 e), revealed a small glass transition at 50.7 °C. The endothermic peak was shown at 181.3 °C and 233.0 °C may be related to the melting temperature of PLA and 4-CBS. Whereas the exothermic peak at 255.5 °C may be related to the degradation of m-CS/PLA.

These results indicate that CS/PLA or m-CS/PLA have quite miscibility and contributing to the shifting of melting temperature.

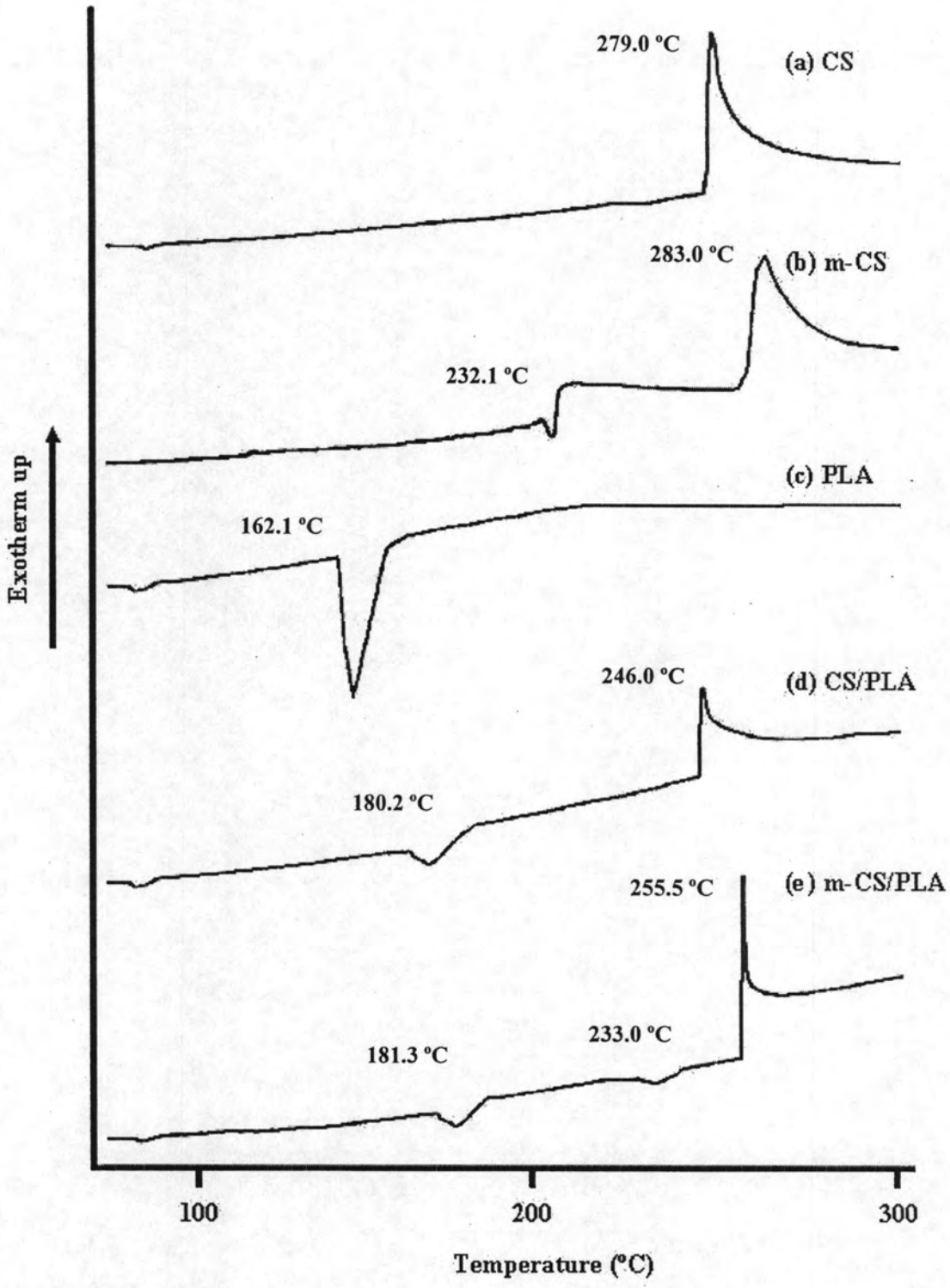

Figure 4.27 DSC thermograms of (a) CS, (b) m-CS, (c) PLA, (d) CS/PLA, (e) m-CS/PLA

4.4.3.5.2 Effect of presenting CS/PLA and m-CS/PLA with DOX

The DSC thermograms of the (CS/PLA)-DOX (1:1 w/w)-1%, (m-CS/PLA)-DOX (1:1 w/w)-1%, (m-CS/PLA)-DOX (2:1 w/w)-1%, (m-CS/PLA)-DOX (1:2 w/w)-1% and (m-CS/PLA)-DOX (1:2 w/w)-2% nanoparticles were shown in Figure 4.28 (Perkin-Elmer DSC7, rate = 10 K/min).

The DSC thermograms of the DOX loaded CS/PLA and m-CS/PLA nanoparticles were displayed in Figure 4.28 (d)-(h). The thermogram of (CS/PLA)-DOX (1:1 w/w)-1% nanoparticles (Figure 4.27 d) showed a small glass transition at 49.4 °C. The exothermic peak at 246.2 °C may be related to the degradation of CS/PLA.

The thermogram of (m-CS/PLA)-DOX (1:1 w/w)-1% nanoparticles (Figure 4.28 e) showed a small glass transition at 48.1 °C. The exothermic peak at 230.9 °C may be related to the degradation of m-CS/PLA. The thermograms of all ratios were quite similar in the shape and positions of the (m-CS/PLA):DOX (1:1):1 nanoparticles.

Therefore, the results showed that all percentage of DOX loaded CS/PLA and m-CS/PLA nanoparticles were similar in the shape and positions of the CS/PLA and m-CS/PLA. Thus, the interactions between CS and DOX were very small and did not significantly affect the thermal properties.

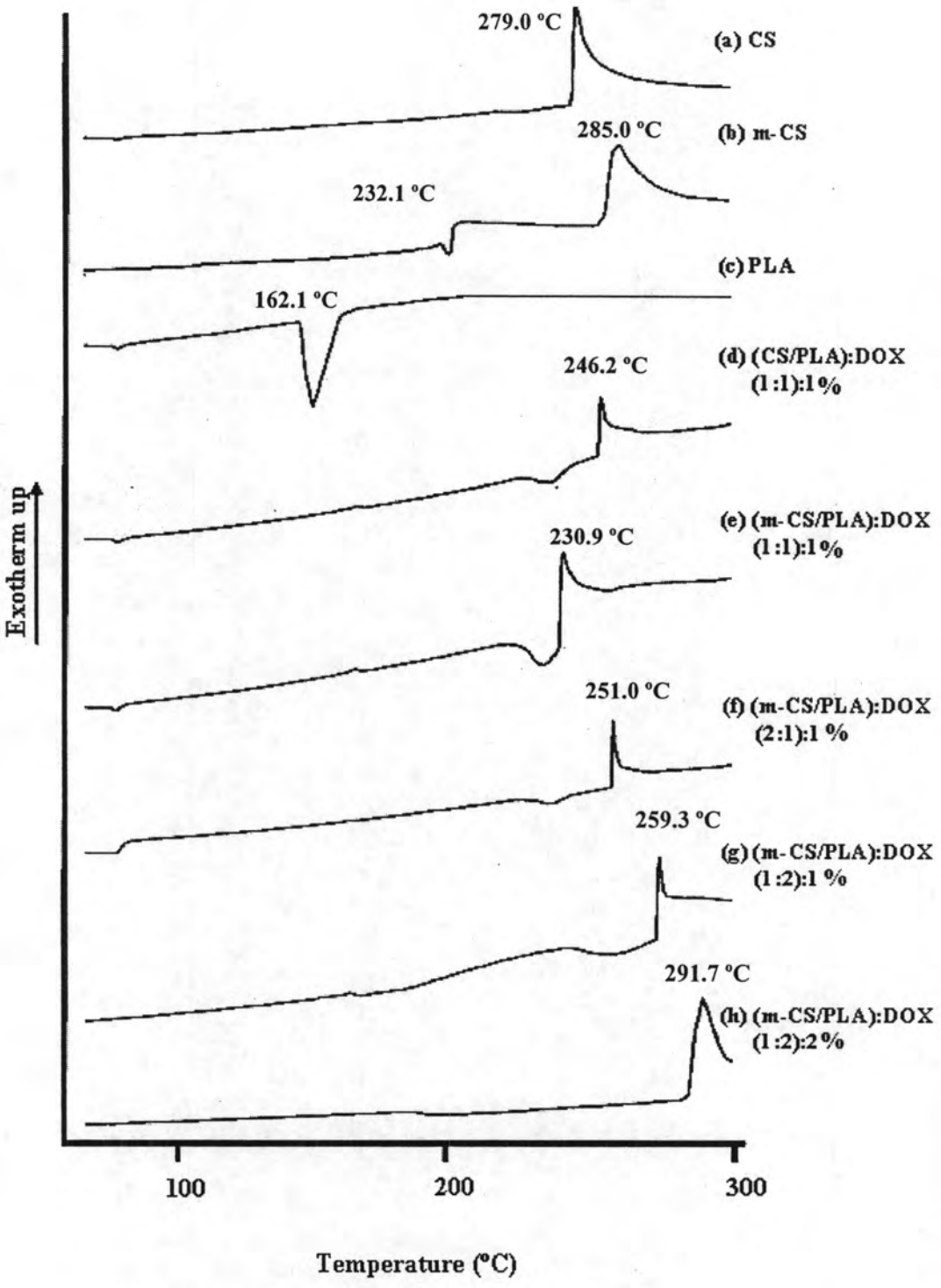

Figure 4.28 DSC thermograms of (a) CS, (b) m-CS, (c) PLA, (d) (CS/PLA)-DOX (1:1 w/w)-1%, (e) (m-CS/PLA)-DOX (1:1 w/w)-1%, (f) (m-CS/PLA)-DOX (2:1 w/w)-1%, (g) (m-CS/PLA)-DOX (1:2 w/w)-1%, (h) (m-CS/PLA)-DOX (1:2 w/w)-2%

4.4.3.6 Thermogravimetric analysis (TGA)

4.4.3.6.1 Effect of presenting chitosan (CS) and m-chitosan (CS) with poly (lactic acid)

The TGA thermograms of CS, m-CS, PLA, CS/PLA and m-CS/PLA nanoparticles were shown in Figure 4.29.

The TGA thermograms of CS (Figure 4.29 a) showed two different stages of weight loss. The first stage range between 30 °C to 150 °C. This may corresponds to the loss of adsorbed and bound water. The second stage of weight loss starts at 157 °C and continues up to 600 °C during which there was 49.5 % weight loss due to the degradation of chitosan with the additional derivative thermogravimetric (DTG) peak at 298.4 °C.

The TGA thermograms of m-CS (Figure 4.29 b) showed two different stages of weight loss. The first stage range between 30 °C to 180 °C. This may corresponds to the loss of adsorbed and bound water. The second stage of weight loss starts at 185 °C and continues up to 600 °C during which there was 55.7 % weight loss due to the degradation of m-CS with the additional derivative thermogravimetric (DTG) peak at 290.3 °C.

The TGA thermograms of PLA (Figure 4.29 c) showed a one stage weight loss. The onset temperature of thermal degragation of PLA is approximately 313.9 °C and the degradation complete at 341.2 °C.

The TGA thermograms of CS/PLA (Figure 4.29 d) showed three different stages of weight loss. The first stage range between 30 °C to 157 °C. The second stage of weight loss starts at 180 °C to 290 °C during which there was 45.5 % weight loss due to the degradation of chitosan with the DTG peak at 242.5 °C. The third stage of weight loss starts at 280 °C to 600 °C during which there was 31.7 % weight loss due to the degradation of PLA with the DTG peak at 340.0 °C.

The TGA thermograms of m-CS/PLA (Figure 4.29 e) showed three different stages of weight loss. The first stage range between 30 °C to 120 °C. The second stage of weight loss starts at 130 °C to 275 °C during which there was 47.6 % weight loss due to the degradation of m-CS with the DTG peak at 238.7 °C. The third

stage of weight loss starts at 280 °C to 600 °C during which there was 32.1 % weight loss due to the degradation of PLA with the DTG peak at 335.5 °C.

The results indicate that no specific interaction between CS or m-CS and PLA and they are quite miscible.

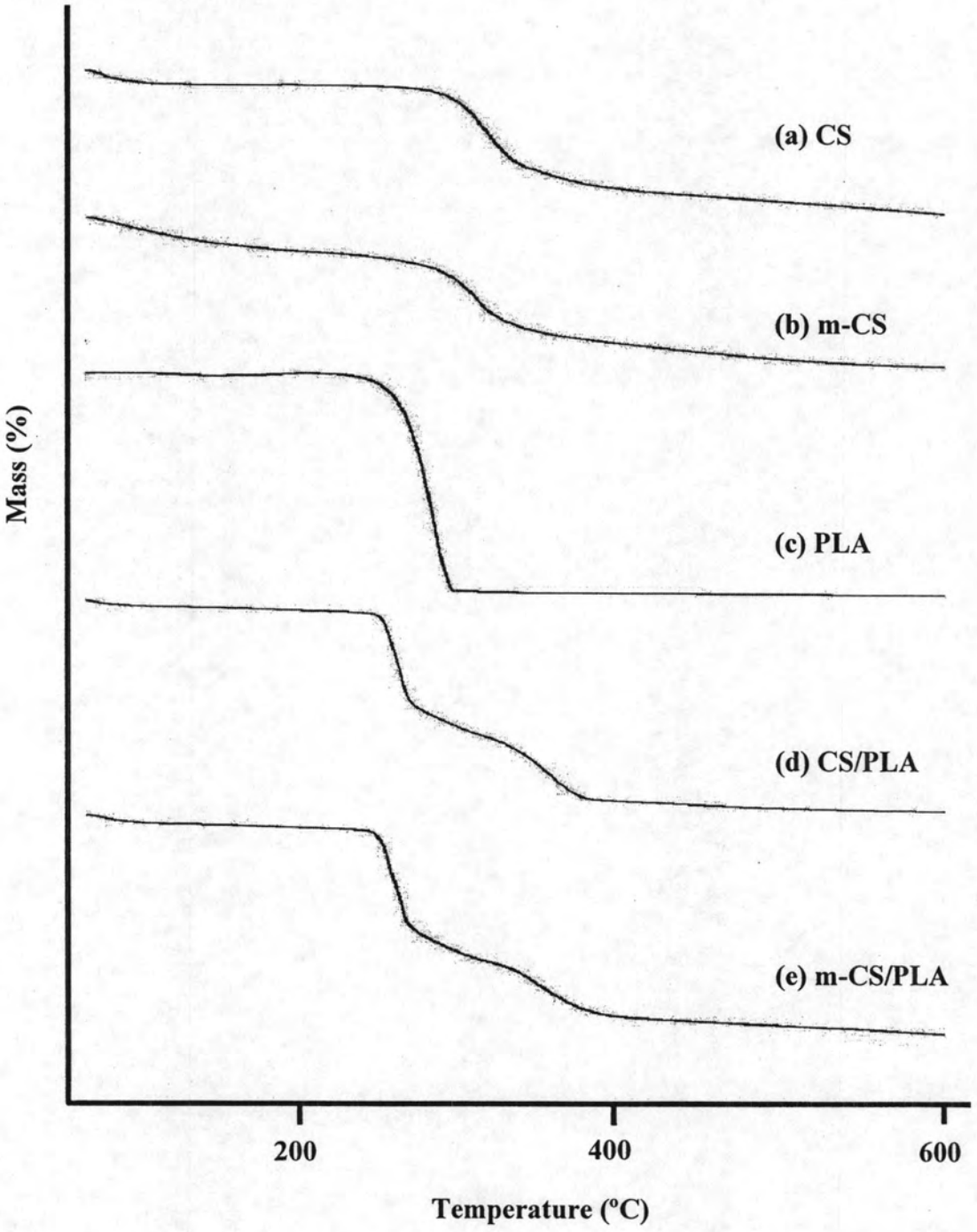

Figure 4.29 TGA thermograms of (a) CS, (b) m-CS, (c) PLA, (d) CS/PLA, (e) m-CS/PLA

4.4.3.6.2 Effect of presenting CS/PLA and m-CS/PLA with DOX

The TGA thermograms of the (CS/PLA)-DOX (1:1 w/w)-1%, (m-CS/PLA)-DOX (1:1 w/w)-1%, (m-CS/PLA)-DOX (2:1 w/w)-1%, (m-CS/PLA)-DOX (1:2 w/w)-1% and (m-CS/PLA)-DOX (1:2 w/w)-2% nanoparticles were shown in Figure 4.30.

The TGA thermograms of (CS/PLA)-DOX (1:1 w/w)-1% (Figure 4.30 d) showed three different stages of weight loss. The first stage range between 30 °C to 120 °C. The second stage of weight loss starts at 125 °C to 268 °C during which there was 43.1 % weight loss due to the degradation of chitosan with the DTG peak at 251.6 °C. The third stage of weight loss starts at 270 °C to 600 °C during which there was 37.5 % weight loss due to the degradation of PLA with the DTG peak at 348.4 °C.

The TGA thermograms of (m-CS/PLA)-DOX (1:1 w/w)-1% (Figure 4.30 e) showed three different stages of weight loss. The first stage range between 30 °C to 120 °C. The second stage of weight loss starts at 125 °C to 270 °C during which there was 48.2 % weight loss due to the degradation of modified chitosan with the DTG peak at 241.2 °C. The third stage of weight loss starts at 275 °C to 600 °C during which there was 30.8 % weight loss due to the degradation of PLA with the DTG peak at 345.6 °C.

The TGA thermograms of formulation of DOX loaded CS, m-CS (Figure 4.30 f-h) are similar to (CS/PLA)-DOX (1:1 w/w)-1% and to (m-CS/PLA)-DOX (1:1 w/w)-1%. The results indicate that the interactions between CS/PLA or m-CS/PLA and DOX were very small and did not significantly affect the thermal properties.

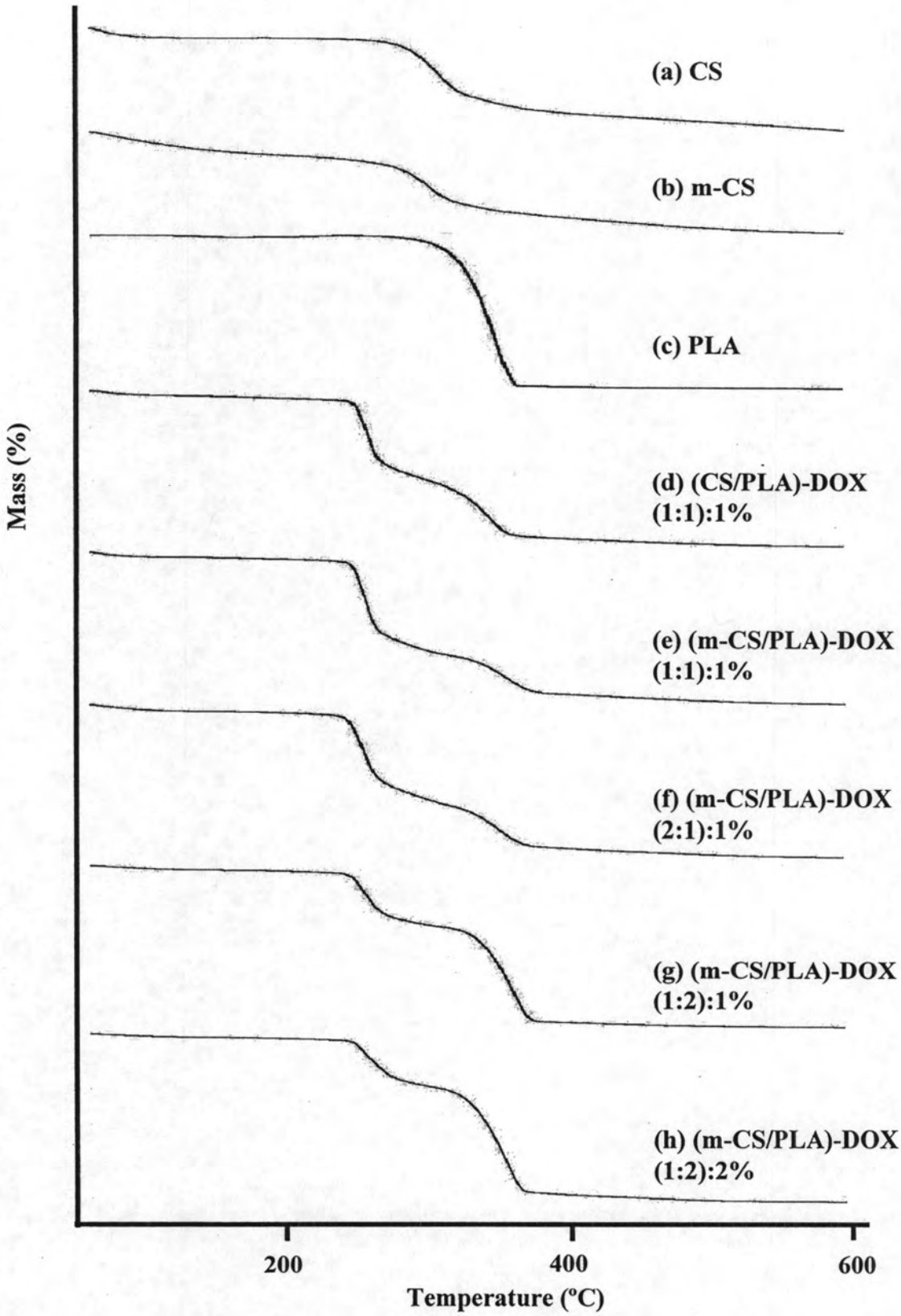

Figure 4.30 TGA thermograms of (a) CS, (b) m-CS, (c) PLA, (d) (CS/PLA)-DOX (1:1 w/w)-1%, (e) (m-CS/PLA)-DOX (1:1 w/w)-1%, (f) (m-CS/PLA)-DOX (2:1 w/w)-1%, (g) (m-CS/PLA)-DOX (1:2 w/w)-1%, (h) (m-CS/PLA)-DOX (1:2 w/w)-2%

4.4.4 Evaluation of drug encapsulation efficiency (%EE)

The percentages of encapsulation efficiency (%EE) of the DOX loaded CS/PLA and m-CS/PLA nanaoparticles were given in Table 4.8.

The encapsulation efficiency of drug within DOX loaded CS/PLA and m-CS/PLA nanaoparticles were analyzed using UV/Vis microplate reader spectroscopy at λ_{max} = 480 nm.

The effect of chitosan and modified chitosan mixed poly (lactic acid) on the drug encapsulation efficiency of nanoparticless were shown in Table 4.8. The encapsulation efficiency of (CS/PLA)-DOX (1:1 w/w)-1% and (m-CS/PLA)-DOX (1:1 w/w)-1% nanoparticles were 60.8% and 64.4%, respectively. It was clearly seen that the efficiency of m-CS to encapsulate the drug was higher than that of the CS (ANOVA, P= $3.37x10^{-3}$).

The effect of modified chitosan mixed poly (lactic acid) on the drug encapsulation efficiency of nanoparticles were shown in Table 4.8. When increasing the amount of m-CS, the %EE was increased from 64.4 and 68.3 %EE. While, the amount of DOX was increasing from 1% to 2% (m-CS/PLA 1:2 w/w), the %EE was significantly increased from 50.2 to 85.8 %EE (ANOVA, P= $9.30x10^{-5}$).

Table 4.8 Encapsulation and loading capacity of doxorubicin loaded polymer nanoparticles*

Formulations	% Encapsulation
• (CS/PLA):DOX (1:1 w/w)-1%	60.8 ± 0.6
• (m-CS/PLA):DOX (1:1 w/w)-1%	64.4 ± 0.8
• (m-CS/PLA):DOX (2:1 w/w)-1%	68.3 ± 1.4
• (m-CS/PLA):DOX (1:2 w/w)-1%	50.2 ± 2.6
• (m-CS/PLA):DOX (1:2 w/w)-2%	85.8 ± 2.9

* mean ± SD (n=3)

4.4.5 In vitro DOX release profiles

4.4.5.1 Effect of CS and m-CS mixed poly (lactic acid) with DOX

The release behavior of DOX from nanoparticles can be described as a graph. The release rate of DOX loaded CS/PLA and m-CS/PLA was given in Appendix B.

The *in vitro* release profiles of (CS/PLA)-DOX (1:1 w/w)-1% and (m-CS/PLA)-DOX (1:1 w/w)-1% nanoparticles were investigated in phosphate buffer solution (PBS, pH 7.4) until 100% of drug was released (18 days) (Figure 4.31). The cumulative release of DOX from (CS/PLA)-DOX (1:1 w/w)-1% showed the two release stages. The first stage, the drug was released about 35% within 8 hours, and then followed the by slower release rate of second stage for 8 days. In case of m-CS/PLA nanoparticles also exhibited two release stages. The first stage, 20% of drug was released within 8 hours. The second stage, the release rate was slower and then sustained to 18 days.

It was clearly observed that (m-CS/PLA)-DOX (1:1 w/w)-1% showed the significantly prolonged release profile of DOX until 18 days when compared with (CS/PLA)-DOX (1:1 w/w)-1%. Thus, m-CS was selected for further studies to improve the release profile.

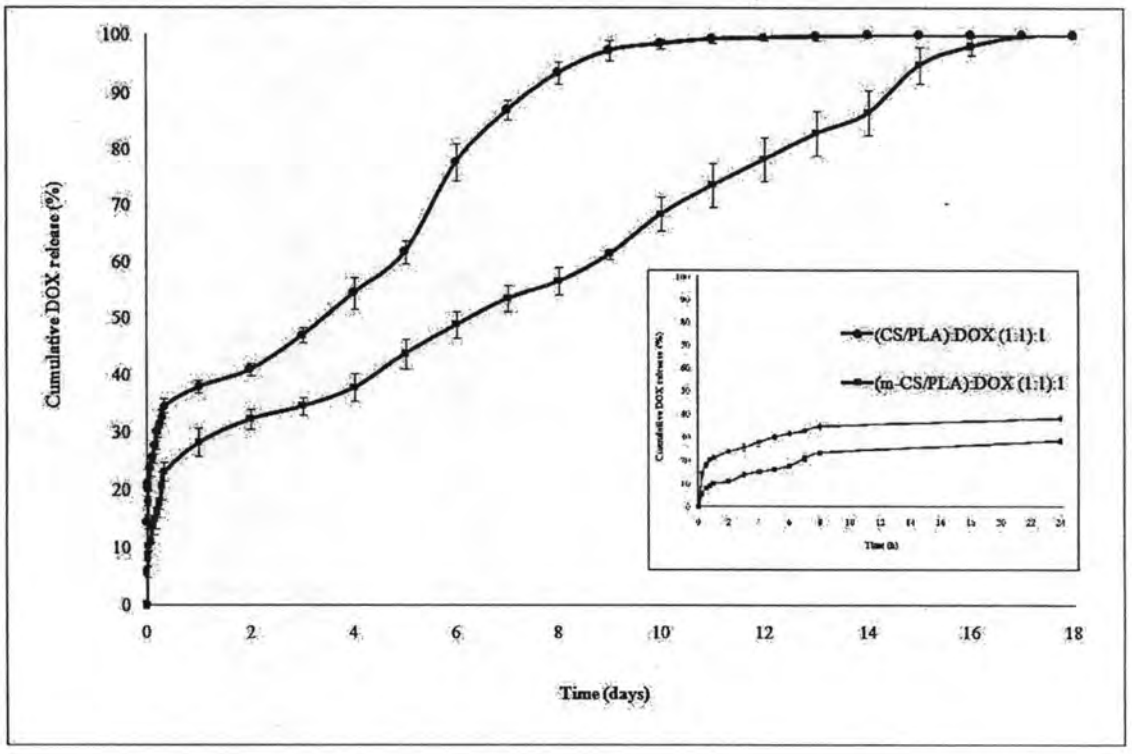

Figure 4.31 Release of doxorubicin (DOX) from CS/PLA and m-CS/PLA nanoparticles at pH 7.4, 37°C (average± SD, n=3)

4.4.5.2 Effect of m-CS and poly (lactic acid) with DOX

The release rate of DOX loaded (m-CS/PLA):DOX (2:1 w/w)-1%, (m-CS/PLA)-DOX (1:2 w/w)-1% and (m-CS/PLA)-DOX (1:2 w/w)-2% was given in Appendix B.

The *in vitro* release profiles of (m-CS/PLA)-DOX (2:1 w/w)-1%, (m-CS/PLA)-DOX (1:2 w/w)-1% and (m-CS/PLA)-DOX (1:2 w/w)-2% nanoparticles were investigated in phosphate buffer solution (PBS, pH 7.4) until 100% of drug was releasd (Figure 4.32). Those of formulations showed the sustained release profiles. The (m-CS/PLA)-DOX (2:1 w/w)-1% nanoparticles exhibited nearly 50 % and 80 %

within 10 and 15 days and after that there was continuing release. While, the release profiles of the (m-CS/PLA)-DOX (1:2 w/w)-1% nanoparticles exhibited nearly 50 % and 80% within 17 and 22 days and and DOX was still sustained released. It was observed that release rate of (m-CS/PLA)-DOX (1:2 w/w)-1% slower than (m-CS/PLA)-DOX (2:1 w/w)-1% nanoparticles. When increasing the amount of PLA, the release rate was slower and prolonged release from days 18 to 26 days Therefore, (m-CS/PLA)-DOX (1:2 w/w)-1% nanoparticles was selected for further studies.

When increase the loaded of DOX, the period of release time were the same (26 days) but the release rate was faster because higher loaded of DOX.

It was obvious that the cumulative release of doxorubicin increased with increasing amount of doxorubicin in the formulation. Higher level of doxorubicin corresponding to lower level of the polymer in the formulation resulted in an increase in the cumulative percentage release. As more drugs were released from the nanoparticles, more channels were produced, contributing to faster drug released. In addition, higher drug levels in the nanoparticles formulation produced a higher drug concentration gradient between the nanoparticles and dissolution medium, thus the cumulative release of drug was increased [66].

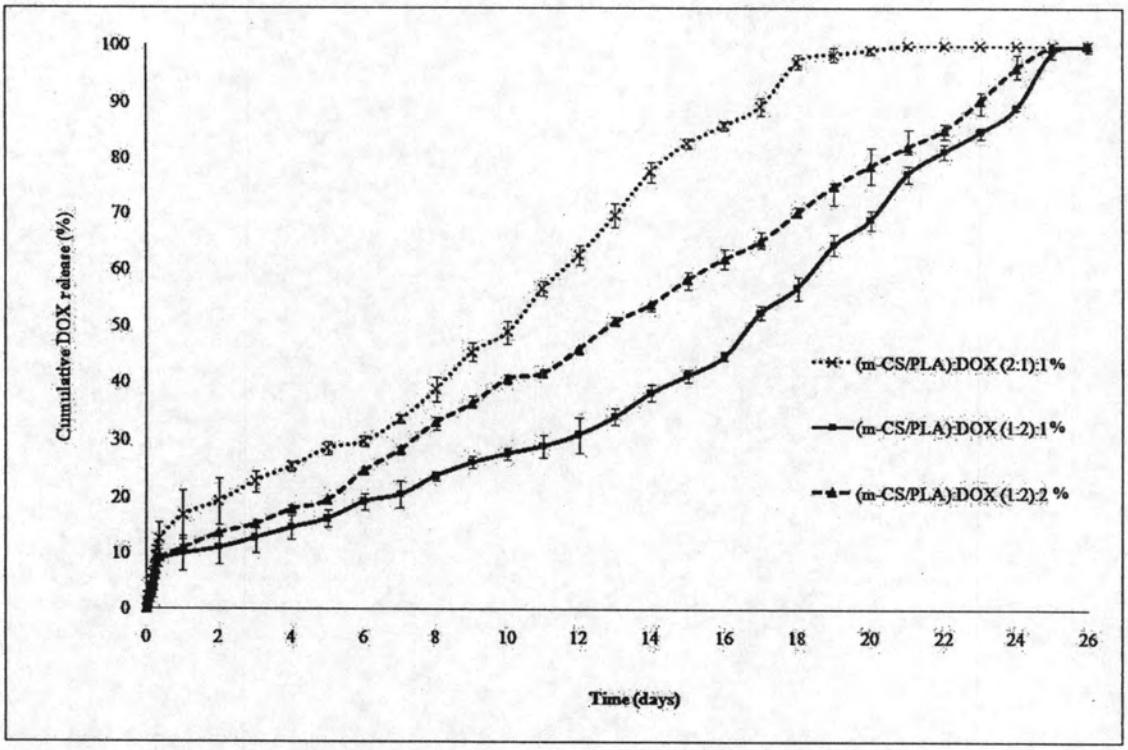

Figure 4.32 Release of doxorubicin (DOX) from (m-CS/PLA)-DOX (2:1 w/w)-1%, (m-CS/PLA)-DOX (1:2 w/w)-1% and (m-CS/PLA)-DOX (1:2 w/w)-2% nanoparticles at pH 7.4, 37°C (average± SD, n=3)

4.4.6 Preparation of pBR322 plasmid DNA

pBR322 Plasmid DNA was prepared from gram-negative bacteria (*E. coli* HB101). FastPlasmid® mini was used for precipitation and separation of plasmid. The *HindIII*-digested λ DNA (commercially obtained) was used as a marker (100 bp-1 kb). The resulted products were analyzed by 1% agarose gel electrophoresis. The obtained plasmid DNA composed of both nicked DNA form and supercoiled pBR322 form (Figure 4.33). Plasmid sizes were calculated using computer software (*Syngene*-Gene Genius, Bio Imaging Systems, *Syngene*). The mobility of supercoiled form corresponds to the marker with 4.3 kb.

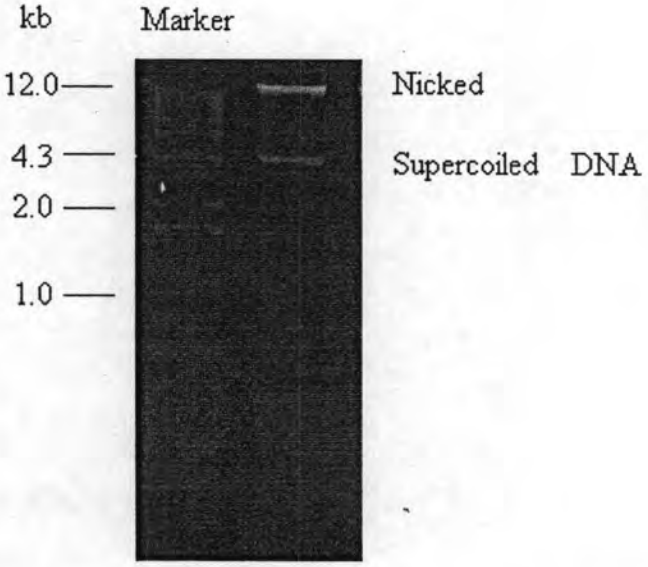

Figure 4.33 Representative of agarose gel profile of pBR322 plasmid DNA band

4.4.7 Topoisomerase II assay

Topoisomerase II inhibition by polymer-DOX nanoparticles

Topoisomerase II is nuclear enzyme that catalyzes changes in the topological state of DNA by breaking and rejoining of double stand DNA. This enzyme has important roles in DNA metabolism such as replication, recombination, transcription, and chromosome condensation. As the structure of DNA is a double helix and is in a supercoiled DNA form. The supercoild DNA must be relaxed by Topoisomerase II

enzyme before processing the transcription and translation. To investigate the effect of the polymer-DOX nanoparticles for inhibiting the relaxation of Topisomerase II was evaluated. The data were analyzed and %inhibition was calculated using Syngene software [67]. The results of topoisomerase II inhibiton of tested compounds and etoposide are shown in Figure 4.34, respectively.

To further investigate the activity of DOX in the nanoparticles, the relaxation of supercoiled pBR322 plasmid DNA by topoisomerase II were evaluated using etoposide, a commercial topoisomerase II inhibitor, as a positive control (Figure 4.34). The topoisomerase II assay was performed with the tested compound concentration of 100 μM and then monitored by 1% agarose gel electrophoresis. In Figure 4.32, the first lane is the *HindIII*-digested λ DNA marker, lane 2 is DNA alone, lane 3 is DNA + Topo II + etoposide as a reference and lane 4 is DNA and Topo II. The results showed that etoposide inhibited 68.76% of Topo II reaction. Whereas, polymer-DOX nanoparticles (**1** to **5**) inhibit 29.67%, 47.26%, 61.24%, 67.53%, and 78.69% of Topo II reaction, respectively (Appendix C).

As results of Topoisomerase II inhibition showed that the DOX loaded nanoparticles still had strong topoisomerase II inhibitory activity.

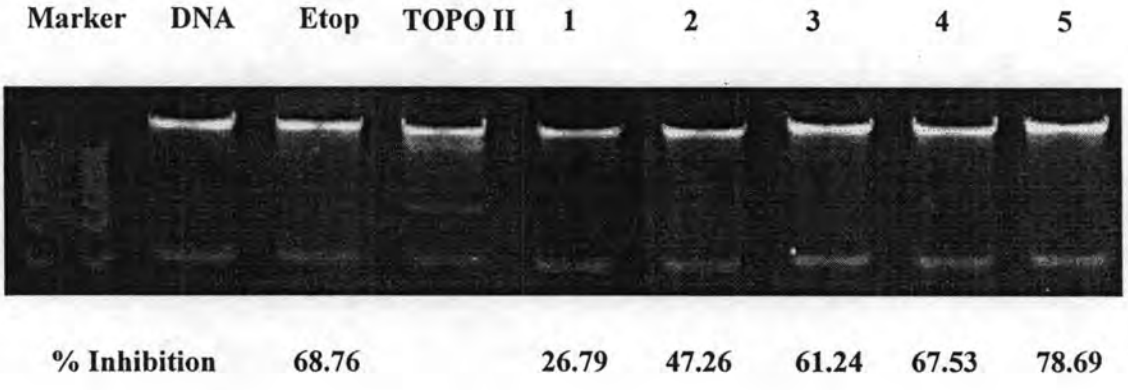

Figure 4.34 Inhibitory effects of tested compounds on human DNA topoisomerse II (lane **1**: (CS/PLA)-DOX (1:1 w/w)-1%, lane **2**: (m-CS/PLA)-DOX (1:1 w/w)-1%, lane **3**: (m-CS/PLA)-DOX (2:1 w/w)-1%, lane **4**: (m-CS/PLA)-DOX (1:2 w/w)-1%, lane **5**: (m-CS/PLA)-DOX (1:2 w/w)-2%)